UNIVERSITY OF
Southampton

FACULTY OF PHYSICAL SCIENCES AND ENGINEERING

Optoelectronic Research Centre
<u>Master of Philosophy</u>

Light

"Exploiting Spontaneous Raman Scattering in Hollow Core Anti-resonant and Photonic Bandgap Fibres for Simultaneous and Multi-Species Quantitative Gas Sensing"

Maria Giovanna Pappa

SUPERVISORS:
Prof David Richardson
Dr Marco Petrovich
Dr Natalie Wheeler

Index

List of Figures

Introduction

The aim of the work described in this thesis is the development of a gas sensor, capable of high sensitivity and selectivity. Particularly, the requirement was for an instrument that could detect and distinguish gases in a mixture, even the ones with low concentration (e.g. 380ppm of CO_2 in ambient air). This work was carried out as part of a collaborative project with IS-instruments, a company whose expertise are the design, development and manufacturing of spectrometers for remote and compact sensor applications. A key application area identified by IS-Instruments is in gas pipelines where the pressure of the gas mixture to be tested can reach 90 bar, so a further requirement on the sensor design was the potential for high pressure operation.

One of the most studied and exploited spectroscopic techniques is Raman spectroscopy, based on Raman scattering. When applied to gas sensing, it can achieve real-time and simultaneous detection of single gases in a mixture. Several research groups have tested this techinque for a wide range of applications, from the industrial field, like the one Is-instruments is interested to develop, to the medical or environmental fields, like breath analysis, or pollution control (some examples can be found in references [1-7]).

Raman scattering can be produced when a monochromatic beam hits matter, like a molecule in a gas. The scattered radiation might have the same frequency of the excitation radiation (Rayleigh scattering) or a shifted frequency (inelastic scattering) that may be caused by some change in the vibrational or rotational state of the molecule; when this happens, the scattered light is called Raman scattering. The energies required to produce such changes are fixed for the type of molecule under observation, meaning that every species needs a defined amount of energy to produce the vibrational or the rotational state change. The so-called Stokes and anti-Stokes Raman lines, shifted towards lower and higher frequency respectively from the excitation one, are the results of those energy changes and are species-specific. Thanks to this property, Raman spectroscopy can be used to distinguish one gas from another so it meets the requirement of specificity for the gas sensor we wanted to develop. However, Raman scattering depends on the scattering cross section of the molecule involved, which has an extremely low value for gases. For instance, considering Nitrogen at room temperature and pressure contained in a transparent cell in which a laser source of ~100 mW at 785 nm is focused (free-space setup), the order of magnitude of the Raman Stokes power is $\sim 10^{-14}$ W, as the scattering cross section of N_2 at 785nm is equal to 7.467×10^{-32} cm^2/sr·molecules [8]. A key limiting factor in the free-space experiment is the interaction length between the gas sample and the laser beam, which is just ~ twice the Rayleigh length of the focused beam [9].

A promising solution to increase this interaction length is based on the use of hollow core photonic crystal fibres (HC-PCFs). The periodic cladding structure of these type of fibres allows the guidance in the lower refractive index hollow core. The possibility to introduce the gas under analysis into the guiding core of a HC-PCF, enables long interaction lengths between the light and the sample and a much more compact device than in a free space arrangement. The Raman signal strength (Stokes power) obtainable using this technique can be hundreds of times higher than what can be obtained in free-space [1]. Furthermore, the fibres can act like

probes for remote gas detection, an important requisite when it comes to environments in which it is necessary to control and detect dangerous or explosive gases, like the gas pipielines.

In this thesis, we investigate the use of HC-PCFs for Raman based gas sensing and develop a sensing scheme which has the potential to meet the necessary requirements of high sensitivity, high selectivity and high-pressure operation. A key part of this work is the comparison of the performance of two different types of HC-PCFs in our sensing scheme.

We will expose the results of experiments based in the use of the so-called photonic bandgap fibres (PBGFs), in which the photonic bandgap created by the periodic cladding is used to guide the light [10, 11]. Furthermore, for the first time we report the use of the so-called anti-resonant (or Kagome) HC-PCF, a type of hollow core fibre never used before in spontaneous Raman spectroscopy [12]. The motivation behind this comparison is that these two fibres types have different physical and optical properties which may or may not provide advantages for Raman gas sensing. For example, the guidance mechanism in anti-resonant fibres, allows for wider transmission windows than the ones achievable in PBGFs which has potential advantages in enabling simultaneous detection of gas species with widely different Raman shifts. In addition, there is more flexibility in the choice of the core size in an anti-resonant fibre and as larger cores can lead to faster loading of samples this can be important in the final application. Being part of a research group in which the hollow core fibres are constantly designed and fabricated, we have been able to employ custom-made fibres to well suit the requirements of the project.

The report is divided in three sections plus the conclusion. In chapter 1, the fundamental theory behind Raman Effect and the hollow core fibres will be discussed. Moreover, the chapter will present a comparison between different spectroscopy techniques for gas sensing and the advantages of Raman spectroscopy based on hollow core fibres. In chapter 2, the setup used for the experiments and the reasons behind the choice of every component and parameter will be explained. Finally, the last chapter (chapter 3) will expose and analyse the results of the experiments that have been completed so far.

1 Background and review of the state of the art

1.1 Introduction to Gas Sensing Techniques

Gas sensing is a field of interest for both academia and industry and it has applications in many different areas. Detection of gases, like CO_2 or Methane, is important in private residences, but also in several industry processes, where there could be also presence of dangerous gases. Fast detection of leakages is important to save human lives and prevent pollution. Furthermore, gas-sensing techniques are widely used in medical applications (e.g. breath analysis or electronic noses).

The aim of the present project is the development of a Raman gas sensor based on hollow core fibres. The key concept is that light from a pump laser is coupled into the hollow core of the fibre which also contains the gas sample; The interaction between the laser beam and the gas sample produces shifted frequencies called Stokes and anti-Stokes frequencies that are specific of the gas species and can provide quantitative information on the gas (or gas mixture) inside the fibre. As we are dealing with an optical sensing technique, we will focus on this kind of gas sensing methods. For the sake of completeness, Appendix A includes a brief discussion on electronic gas sensing techniques.

Two family of optical techniques can detect single gases from a mixture: those based on optical absorption (especially in the IR) and those based on Raman scattering. Infrared (IR) and Raman spectroscopy are both optical methods based on the change of the vibrational state of a molecule. They are used to identify which substances are contained in a sample and the relative amount. Furthermore, IR and Raman sensing, give information about the chemical structures and physical form of the molecule thanks to "fingerprint" spectral patterns [13].

Gas-based Raman spectroscopy is not as widespread as IR spectroscopy. As will be explained in the next section, Raman scattering is a weak effect, due to the small value of the scattering cross section of gases [14], and it needs high excitation powers. However, the availability of powerful lasers and the development of products cheaper than in the past, are making this technique more and more appealing for both industries and academia.

In the following section, a selection of methods based on optical detection of gases will be described. Raman spectroscopy, the technique used in this project, will be discussed in detail; it will be compared with the IR techniques that, currently, are most used in the fields of interest of this project.

1.2 Gas Sensing based on Optical Absorption

Many gases used in the industry and many important environmental gases (e.g., CO, CO_2, CH_4, NO_2, O_3, NH_3, H_2S) show absorption lines in the UV-visible and near-mid infrared (NIR and mid IR) regions. The absorption lines or bands are specific to each gas and their detection is based on this concept.

For this reason, gas sensing based on optical absorption is widely spread. The mid IR region is particularly interesting, because many species show absorption spectra in this region. Optical absorption spectroscopy is based on the Beer-Lambert law (considering a monochromatic source):

$$I_{out} = I_{in}e^{-\alpha L} \qquad (1)$$

where:

- I_{out} = Intensity of the output light after the sensing process
- I_{in} = Intensity of the input light
- α = absorption coefficient = εC
- ε = specific absorptivity of the gas
- C = concentration of the gas
- L = optical path length of the light beam through the gas sample

The absorption coefficient is the product of the gas concentration and its absorptivity. If αL is small, equation (1) becomes:

$$\frac{\Delta I}{I_{in}} = absorbance \cong \alpha L \quad (2)$$

where: $\Delta I = I_{in} - I_{out}$

The noise equivalent absorbance (NEA) or the minimum detectable absorption coefficient α_{min}, are used to compare the different techniques based on optical absorption. The absorption spectrum is a plot of α or ε vs wavelength (λ) or wavenumber and, at ambient pressure, a single gas line has a Lorentzian profile (figure 1).

In the following sections, some of the most used techniques based on optical absorption will be briefly discussed.
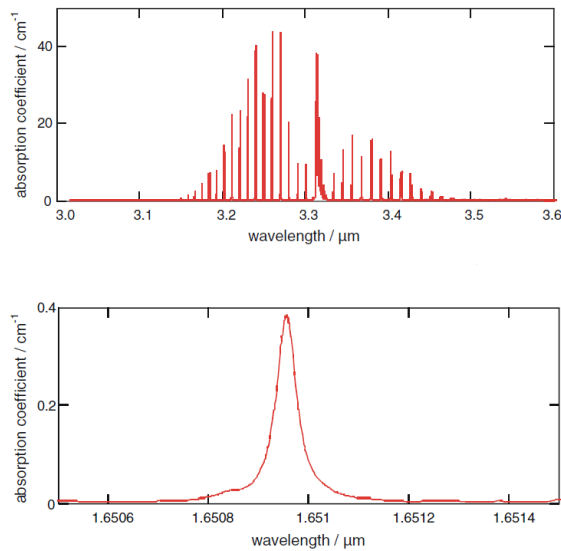
Figure 1 Top: Methane spectrum in the mid-IR [15]. Bottom: Absorption line of Methane at 1.651 μm at 1bar [16].

1.2.1 Non-dispersive sensors

Those sensors are cheap and simple because they are made of few components. They use broadband light sources (like micro bulb) whose emission passes through two filters, one covering the spectral region of absorption of the target gas and the other covering a close wavelength region. The second filter is used to obtain a reference to compensate for changes in the source emission.

Thanks to the strong optical absorption in the mid-IR region, non-dispersive sensors reach good values of sensitivity (around 10-50 ppm for CO_2). By using more sophisticated equipment, like a cooled detector, they can also reach sensitivities ~ 1ppm [17].
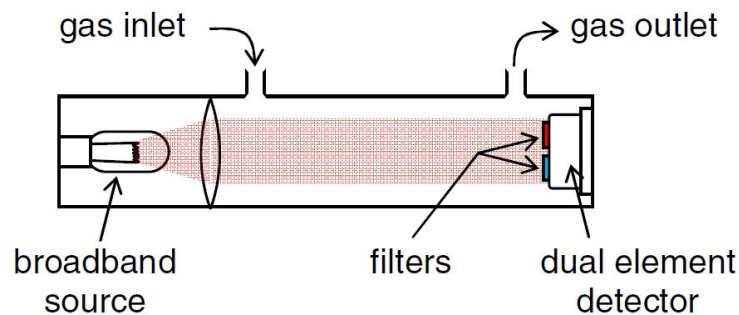
Figure 2 Schematic of a non-dispersive gas sensor [17].

1.2.2 Tuneable diode laser spectroscopy (TDLAS)

In TDLAS, a single narrow line from a tuneable laser is scanned across the absorption wavelength range of the gases we want to detect (see figure 3). Two techniques are used for this kind of spectroscopy: direct spectroscopy and wavelength modulation spectroscopy (WMS).

The direct detection is obtained by ramping the injection current of the laser to tune the wavelength over the range of interest. Since the laser intensity rises with the increasing current, the output will show a rising background with a dip that corresponds to the gas absorption. The absorption alone can be recovered by subtracting a zero reference or by a ratio between input and output power [17].

In WMS, the injection current is modulated while the laser wavelength is tuned across the absorption region of the target gas. A harmonic spectrum of the absorption line is produced and its intensity is proportional to the concentration of the analyte [18]. To detect the gas, the second harmonic produced by this ac modulation, is typically used; it can be mathematically proved that the peak of the second harmonic correspond to the absorption line centre [19]. To recover the second harmonic, a 2f-lock-in amplifier is added at the receiver stage. Since many diode lasers can be modulated at frequency up to MHz, the procedure can be also very fast.
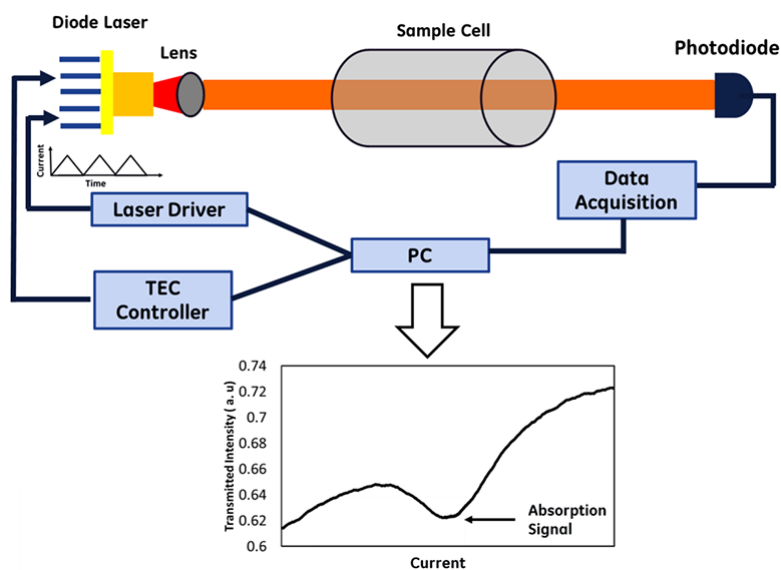
Figure 3 TDLAS direct spectroscopy scheme. The driver current tune the laser but also causes an increase in the intensity. The dip in the transmitted intensity graph corresponds to the gas absorption wavelength [20].

TDLAS has the main advantage of a high signal to noise ratio. This kind of detection is in fact self-referenced: the output spectrum is referenced with the input laser spectrum, so it is possible to compare the central peak absorption with the "zero" level on each side of the line.

The best sensitivity reached in the wavelength modulation TDLAS is ~1ppm [21]. Moreover, thanks to the narrow laser line, it is possible to obtain high level of specificity for the gas under test, this means it might be possible to catch it from a mixture of other gases (for instance Methane in a mixture of other hydrocarbons) [17].

1.2.3 Photoacoustic Detection

This technique exploits the conversion of the light energy into heat: the light source hits the sample and the produced heat causes the expansion of the sample. By modulation of the light, it is possible to produce pressure waves and to detect them with a microphone. The scattered light, one of the issue with the conventional spectrometry, has less impact on the photoacoustic signal. Furthermore, the detected signal is proportional to the intensity of the light absorbed rather than the transmitted radiation. However, those sensors are highly sensitive to the vibrations of the background, which cause noise. In the field, this noise can be unpredictable and it varies from site to site [17].

1.3 Raman Spectroscopy

1.3.1 Introduction

Many indicators can be used to judge a gas technique. The sensitivity, i.e. the minimal amount of gas that the detector can sense is a key factor when it comes to the detection of small amount of gas concentration in a mixture. Furthermore, the selectivity of the sensor, i.e. the range of gas that can be detected by the same instrument, is fundamental. Some techniques can just detect specific range of gases. In the detection of CO_2, for instance, the non-dispersive infrared sensors reach a sensitivity of ~10-50ppm. However, they can cover only a region of the spectrum close to the target gas (see 1.2.1).

We had to choose a competitive sensing technique that could be able to detect single gases of a mixture for in-field and remote detections at the same time (in the pipeline, for instance, only a remote control is possible).

TDLS have good SNR and high level of selectivity, as already reported in 1.2.2. However, they need a tuneable source to scan the wavelength range of interest, while Raman spectroscopy, can rely on the use of a single wavelength source and Raman shifts do not depend on the excitation frequency. Moreover, the shifts are species-specific and act like fingerprints for the materials under test.

As will be discussed in the next sections, Raman scattering from gases can be weak and high laser power might help to have a stronger signal. Another parameter that can be used to improve Raman intensity, is the interaction length between the gas and the light [13, 22-24]. While bulky gas cells have been widely used, in the last few years researchers have investigated the use hollow photonic bandgap core fibres (HC-PBGFs) as alternative gas cells which simultaneously guide the pump laser light and confine the gas sample allowing them to interact for the whole fibre length. In 2008, M. Buric et al. proved an increment of more than 130 times in the Raman signal by using 1.5m of photonic bandgap fibre compared with a free space arrangement [1]. The fibre was filled with ambient air at ambient pressure and the exciting laser source was a 514.5nm TEM_{00} Argon-ion laser.

In the following years, several research groups have proved that hollow core fibres can be efficiently used in Raman spectroscopy [1-6]. Table 1, at the end of this chapter, shows a

comparison between some of the main experiments in the latest years using hollow core photonic bandgap fibres (PBGF) for Raman gas sensing.

We decide to adopt Raman spectroscopy as sensing technique for our project and, for the first time, we used a HC-PCF whose operation is not based on photonic bandgap guidance. This fibre, the "Kagome fibre", works thanks to an anti-resonance effect that make possible to guide the light mainly in the hollow core. As will be explained in 1.5, the broad bandwidths, together with more flexibility in the core size, which can lead to faster gas filling, makes the Kagome fibre a promising tool for Raman spectroscopy.

The next two sections will discuss the theory and the main equations of the Raman Effect, on which Raman Spectroscopy is based.

1.3.2 The Raman Effect

When a monochromatic radiation of frequency ω_1 interacts with matter (in solid, liquid or gaseous state), some light is absorbed or transmitted by the material and some is scattered. Rayleigh scattered light has the same frequency of the incident beam and for this reason, it is classified as "elastic" scattering. However, analysing the content of the scattered light, light at different frequencies than the exciting source can be observed. This kind of scattering is the Raman scattering, named after the scientist who discovered it, an "inelastic" effect. Light lines at lower frequencies than the monochromatic radiation ω_L are called Stokes line, lines with higher frequency value are called anti-Stokes lines. Those lines are specific to every species [22, 24] acting like fingerprints for the materials under test. For this reason, Raman spectroscopy permits high selectivity allowing, for instance, the detection of single gas species in a gas mixture.

To be Raman-active the molecules need to be polarizable and to lack a permanent dipole. The effect induces change in the vibrational or rotational (or both) state of a molecule and this variation must also produce change in the polarizability [22, 24], this is the case of all diatomic molecules, like Oxygen and Nitrogen. The mutual exclusion rule applies for polyatomic molecules: vibrations, which are active in the infrared spectrum, are not active in the Raman spectrum and vice versa. For mononuclear diatomic molecules, such as N_2 and O_2, and symmetrical linear polyatomic molecules, such as acetylene and cyanomethylene, only Raman spectroscopy can be used for investigation of rotational spectrum (no dipole moment and so infrared spectroscopy is not possible) [25].

The scattering cross section, i.e. the effective area of collision between the photons and the material under test, is a fundamental parameter that affect the intensity of the scattered radiation. Relative Raman scattering cross sections of gases measured with laser excitation have been determined in relation to the Q-branch of the vibrational Raman band of Nitrogen, because N_2 is non-reactive and can easily be mixed with other gases to serve as an internal standard. Figure 4 shows relative differential cross sections of several gases, obtained with this technique.
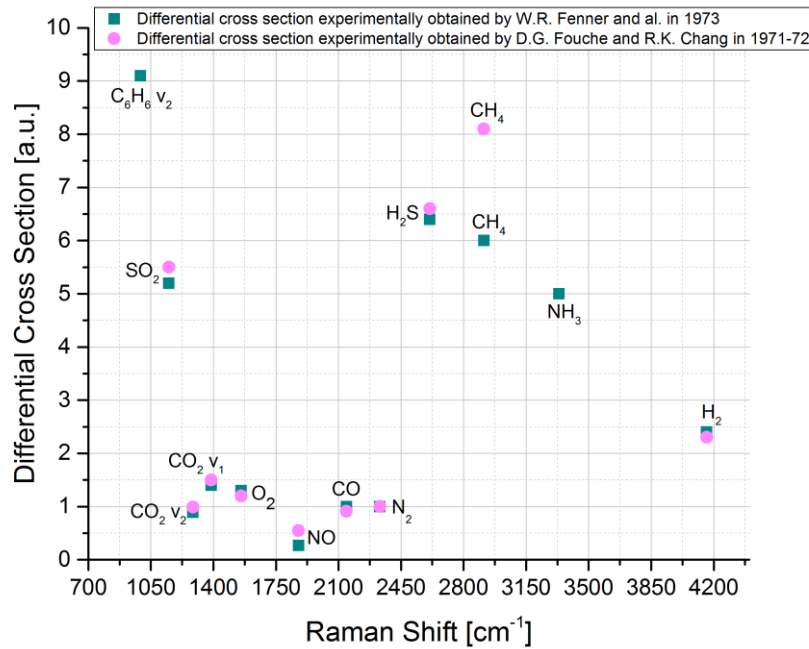
Figure 4 Relative differential cross sections for different gases versus Raman frequency shifts [26, 27] [28].

The absolute differential scattering cross section of the vibrational line of Nitrogen at 488 nm has found to be 4.3×10^{-31} cm^2/ster-mol [14]. This low value of the scattering cross sections in gases, is the main drawback of the Raman spectroscopy as it causes the Raman signals to be weak (with power levels in the order of pWs), as can be seen from equation (10) in the next section. Therefore, Raman spectroscopy of a gas usually involves high laser power (hundreds of mW to several Watt) or a multi-pass arrangement where the illumination laser beam is focused on the sample volume from a variety of directions.

1.3.3 Raman Theory

To have a better understanding of the Raman Effect, this section will expose the equations behind Raman theory that lead to the final expression of the intensity of the scattered radiation. When an electromagnetic field interact with matter, it induces a dipole moment expressed as [22]:

$$\vec{P} = \alpha\vec{E} \quad (3)$$

where:

$\vec{P}$= Induced dipole
$\vec{E}$= Electric field
α = Polarizability of the material

16

Both P and E are vectors, so the polarizability α is a tensor; it can be diagonalized and then visualized in terms of polarizability ellipsoid, with the three axes being α_X, α_Y, α_Z. The polarizability ellipsoid changes when there is a molecular vibration that causes a displacement from the equilibrium position, of the atoms nuclei of a molecule. An example for Carbon dioxide is shown in figure 5.
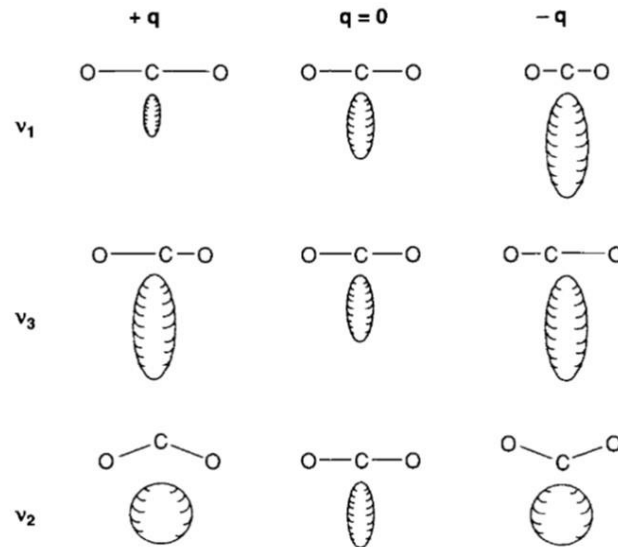
Figure 5 Vibration modes of CO_2 molecule causing changes in the polarizability ellipsoid [23].

Considering small displacements of the nuclei compared with the internuclear distance, each component of the polarizability tensor can be written as a series expansion in the nuclear coordinate system:

$$\alpha_{ij} = \alpha_{ij,0} + \sum_k \left(\frac{\partial \alpha_{ij}}{\partial \xi_k}\right)_0 \xi_k + \cdots \quad (4)$$

Where ij can be x, y, z, and the sum, considering all the changes from the equilibrium position of the nuclei. ξ_k is the normal coordinate of vibration associated with the molecular vibrational frequency v_k [24]:

$$\xi_k = \xi_{k,0} cos(2\pi v_k t) \quad (5)$$

Considering an oscillating electric field of frequency v:

$$E = E_0 \cos(2\pi v t) \quad (6)$$

We can substitute in (3) obtaining [29]:

$$P_j = \sum_i \alpha_{ij,0} E_0 \cos(2\pi v t) + \frac{1}{2} \sum_{kj} \left[\left(\frac{\partial \alpha_{ij}}{\partial \xi_k} \right)_0 E_{j,0} \right] \xi_k \{ \cos[2\pi(v + v_k)t] + \cos[2\pi(v - v_k)t] \}. \quad (7)$$

Equation (7) is divided in three parts, representing the induced oscillating dipoles; the first one describing Rayleigh scattering, oscillates with the same frequency ν of the incident radiation. The other two other blocks lead the inelastic Raman scattering at frequency ν+v_k (anti-Stokes) and ν-v_k (Stokes).

Let us consider the corpuscular nature of the light for a better understanding the phenomena. If there are N photons, each with energy $\hbar\omega_L$ hitting a molecule whose initial energy state is E_i, the interaction between the radiation and the molecule could lead to the creation of a new photon with energy $\hbar\omega_s$ and the annihilation of one photon with frequency ω_L.

As the energy must be conserved, now the molecule is in a new energy state $E_f = E_i + \hbar\omega_f$, where $\omega_f = \omega_L - \omega_S$. The light scattered from the molecule has (N-1) photons with energy $\hbar\omega_L$ and one photon of energy $\hbar\omega_s$. If E_f is lower than E_i, then the new photon has frequency $\omega_S > \omega_L$ and we have anti-Stokes Raman scattering. On the contrary, if E_f is higher than E_i, we have Stokes Raman scattering and the new photon has a frequency $\omega_S < \omega_L$ (or $\lambda_S > \lambda_L$ if we consider the wavelengths). In figure 6, it is possible to see a diagram of this process.
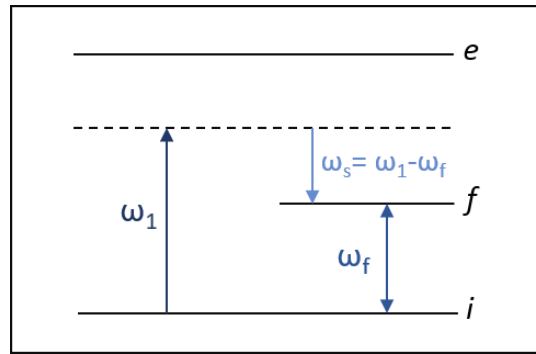
Figure 6 Energy diagram of the transitions involved in Raman Scattering: ω_1 is the pump frequency, ω_s is the frequency of Raman scattered photon and f is the final energy state of the molecule.

The cross section express the Raman scattering efficiency of a molecule, that means how probable is the scattering event; it is proportional to the electronic polarizability and has the dimension of an area [30]:

$$\sigma(\omega_{scattering}) \propto \left| \frac{\partial \alpha}{\partial \xi} \right|^2 \quad (8)$$

This means that the condition of a non-zero polarizability change along the nuclear coordinate is required.

The intensity of the Raman signal is proportional to the differential scattering cross section of the molecule, a function that quantifies the intrinsic rate at which the scattered photons can be detected at a given angle, it is given by:

$$\frac{\delta\sigma}{\delta\Omega}(\omega_S) = \frac{1}{9} \frac{(\omega_1 \cdot \omega_S^3)}{\pi^2 \epsilon_0^2 \hbar^2 c^4} Im\{R(\omega_S, \omega_S - \omega_1, -\omega_1)\} \quad m^2/sr \quad (9)$$

where:

- ω_S = frequency of the Raman scattered light.
- $\Delta\omega$ = Raman Shift, this is the difference between the frequency of the exciting light and ω_S.
- $\omega_1 = \omega_S + \Delta\omega$ = Laser frequency.
- R represents the transition rate between the two states |i> (initial state of the molecule) and |n> (excited vibrational or rotational state of the molecule).

Equation (9) shows also that the differential scattering cross section is highly dependent on the frequency of the source. Considering that ω_s is just the source frequency minus the Raman shift, $\frac{\delta\sigma}{\delta\Omega}$ grows as the fourth power of ω_1.

Raman shift exactly defines the vibrational (or rotational) characteristics of a molecule. Therefore, if a species is Raman active, it is possible to understand its nature by its Raman spectrum, which acts like a "fingerprint" for the molecule.

The intensity of Raman lines can be expressed as:

$$I_S = kI_L \rho L \left(\frac{\partial\sigma}{\partial\Omega}\right)\Omega \qquad (10)$$

- ρ = molecular number density in the measurement volume V in molecules/cm^3
- Ω = solid angle observed
- L = length of the measurement volume/ interaction length between the beam and the sample.
- I_L = intensity of the light hitting the molecule
- k = setup constant depending on geometry and wavelength-dependent losses

The linear dependence from L, leads to the advantage of using hollow core fibres as the entire length of the fibre represents the interaction length between the gas contained in the hollow core, and the laser beam.

Using the perfect gases law, we can express the molecular density ρ as:

$$\rho = \rho_{moles} \times N_a = \frac{p}{RT} \times 6.022 \times 10^{23} \qquad (11)$$

Where N_a is the Avogadro number. If we consider equation (10) again and substitute ρ as it is expressed in (11), we can see how the intensity is also pressure-dependent. This means that it could be possible to have higher Raman signal by increasing the pressure of the gas under test [31].

1.4 Photonic Bandgap Hollow Core Fibres

Traditional optical fibres guide light via total internal reflection due to the difference in the refractive index between the cladding and the core materials. In particular, the refractive index of the core has to be higher than the cladding.

Around the 90's, researchers started to demonstrate a new way of guiding the light in a lower refractive index core thanks to a periodic structure of the cladding which forms the so-called "photonic bandgap" [10]. The periodic structure consists of a two-dimensional array of holes surrounding the core for all the length of the fibre [32] and the fibres with this geometry are called Photonic Crystal Fibres (PCFs).

 In 1999 the possibility to guide light in air, and in particular, in a hollow core surrounded by a periodic cladding, was demonstrated [11]. The periodic structure of the cladding, formed by glass rods and connecting struts makes possible the creation of a periodic sequence of forbidden bands (the bandgap, PBG) that extend below the air-line, this is the region of the fibre in which the effective refractive index is one [32, 33]. This PBG presents a range of light frequencies and a set of guided modes with fixed propagation constants for which light cannot travel in the cladding structure. If the core, created by omitting a specific number of rods from the cladding, is designed to support modes in these PBG regions, the light can be confined and transmitted.

Most HC-PBGFs only have one low loss transmission window. Numerical studies have shown that increasing the air filling fraction in the cladding, which means thinner struts, can lead to a broader guidance window. Different lattice arrangements have been tested as well, to have struts as thin as possible. It has been shown, for instance, that a square lattice of holes has ~20% wider bandgap than the triangular lattice of holes (TLH). The broadest bandgap demonstrated for the TLH is around 34% of the operational wavelength [34].

Figure 7, from reference [32], shows the impact of the air-filling fraction on the photonic bandgap. A HC-PBGF with a cladding with a TLH has been considered. Calling D the diameters of the rods and Λ the distance between two centres of the rods (pitch), we can see how increasing the air filling fraction, i.e. having thinner struts, shifts the bandgap towards higher frequency and make it broader.
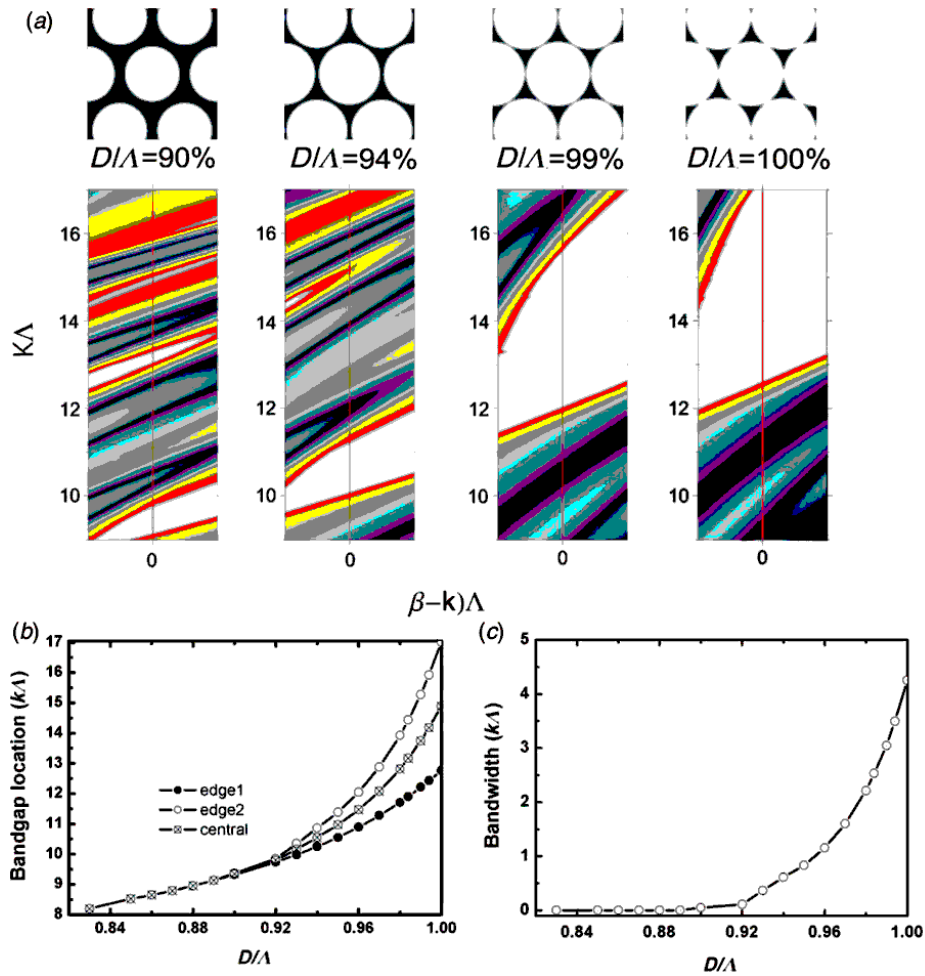
Figure 7 Evolution of the photonic bandgap by increasing the air-filling fraction in the fibre [32].

The core in the bandgap fibres is made by omitting glass rods. With a core made by 19 missing rods, low values of transmission losses (1.2 dB/km@ ~1560nm) have been achieved [35-37]. On the other hand, the abrupt interruption of the periodic cladding causes the so-called surface modes in PBGF that are localized at the core surround [32, 34, 38, 39]. Those modes are lossier than the core modes and they can interfere with them increasing the propagation loss. Figure 8 and 10 show some high attenuation regions in the transmission spectrum of the PBGF that are caused by the surface modes (SMs) located in the core surround. As in a traditional optical fibre, the PBGF should have a finite number of well-confined core modes and infinite cladding modes with high attenuation. Surface modes are something in between as they can be guided in the core but their field intensity is mostly localised in the glass of the core surround. This field extends in the leaky cladding and is considered responsible of the high loss introduced in the bandgap when the SMs anti-cross with the core modes [39-41]. Figure 8 shows the phenomenon: SMs created in the struts and rods of the core surround exist in the bandgap and interfere with the core modes causing the high loss region in the transmission as reported in the bottom of the figure.
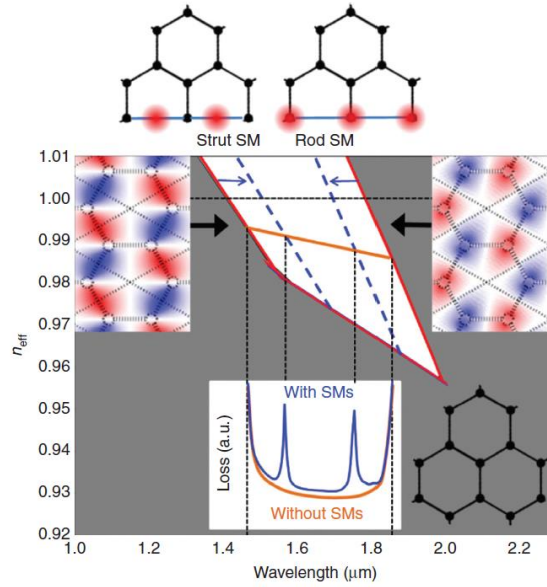
Figure 8 Modes localised in the struts or in the rods of the cladding surrounding the air-core can extend inside the bandgap (white region). These modes, called Surface Modes (SMs), are due to the termination of the periodicity of the cladding to form the hollow core. The Surface Modes can anti-cross the core-modes (orange line) causing loss[34].

It has been proved that SMs anti-cross higher order core guided modes at longer wavelengths than the fundamental mode. SMs anti-crossings with core modes are mode dependant and shifted to longer wavelengths for the LP_{11} modes compared to the LP_{01} fundamental mode, an example of this event is shown in figure 9 for a 37-cell PBGF [34, 40].
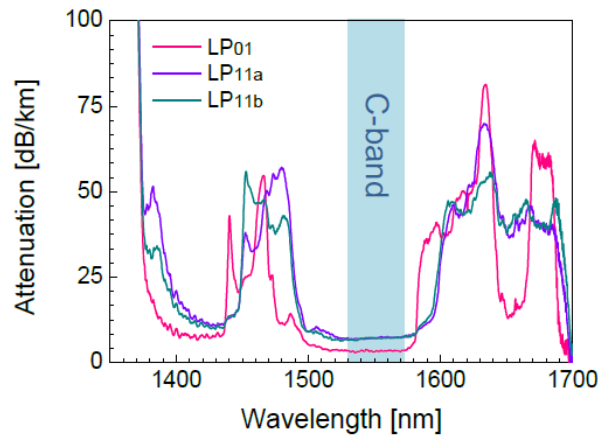
Figure 9 Transmission loss for the LP_{01} and $LP_{11a,b}$ modes of the 37cells PBGF of reference [40].The two peaks of SMs anti-crossings are mode dependant and shifted of ~10nm on the right for the $LP_{11a,b}$ modes.

An important parameter to control this SMs is the thickness T of the boundary of the core. By fabricating fibres with T~ half of the struts average thickness, it is possible to avoid the surface modes [42, 43]. However, to have lower loss, the omission of more capillaries, to create larger core, causes distortions in the core surround that made the complete elimination of surface mode impossible. Figure 10 shows a 19-cells core defect PBGF with the transmission window

located between 800 and 110nm. The presence of surface modes limits the bandwidth (~60-70nm) and increases the propagation loss of the fibre.
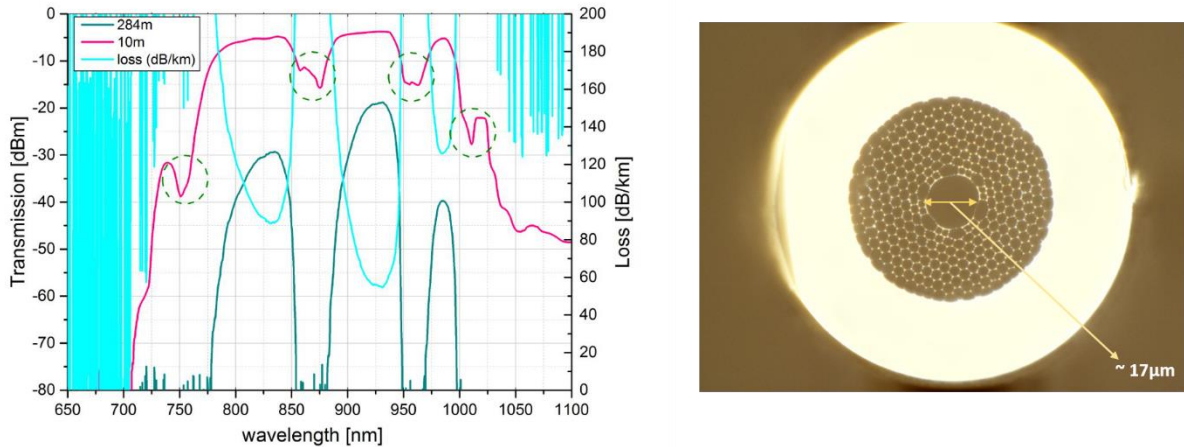
Figure 10 White light source power transmitted by 284m and 10m of the 19-cells HC-PBGF used in the experiments. The green dotted circles indicate the dips due to the surface modes anti-crossing the core modes. The light-blue trace indicates the loss measurement obtained with the cut-back technique from 284m to 10 m. A microscope image of the fibre is shown on the right.

1.5 Kagome fibre

As shown in the previous paragraph, the guidance of the PBGF is usually limited to a single spectral window; the necessity of the glass struts to connect the rods is the cause of this limitation. Furthermore, the presence of surface modes, leads to dips in the transmission (increase of the loss), as shown in figure 8.

However, another kind of hollow core fibre, the anti-resonant Kagome fibre, can be used when broader transmission windows are required. The operation principle of this kind of fibre does not rely on the formation of a photonic bandgap. The cladding structure of Kagome fibre, that resembles that of a "Kagome", a Japanese basket, is made of thin connected glass struts to form a network (see figure 9). These glass bridges can guide modes, thus, to have guidance in the hollow core, we have to transmit with wavelengths located between the cut-off wavelengths of those modes [44]. At the resonant wavelengths, the modes in the core and the modes in the struts of the cladding are in phase matching, and they can interfere with each other. Calling δ the thickness of the struts and n the refractive index of glass, the resonance wavelengths (λ_r) are given by [45]:

$$\lambda_r \approx \frac{2\delta\sqrt{n^2 - 1}}{m} \ , \quad m = 1, 2, 3, \dots \quad (12)$$

Furthermore, while in the PBGF the struts should be as thinner as possible as they narrow the transmission bandwidth, in anti-resonant Kagome fibres, the nodes formed between the struts

should be small. In fact, they have resonances close to the air-line that are different from the ones of the struts and thus limit the width of the transmission windows [32].

To have a better understanding of the operational principle of this kind of fibre and a proof of the existence of the anti-resonance wavelengths, we can look at picture 11, showing a microscope imagine of the output of a 7-cell Kagome fibre illuminated by the white light of the microscope. Each hole of the cladding can guide narrow range frequency of the light, as proved by the different colours of light (meaning different wavelengths) exiting the fibre shown in the picture.
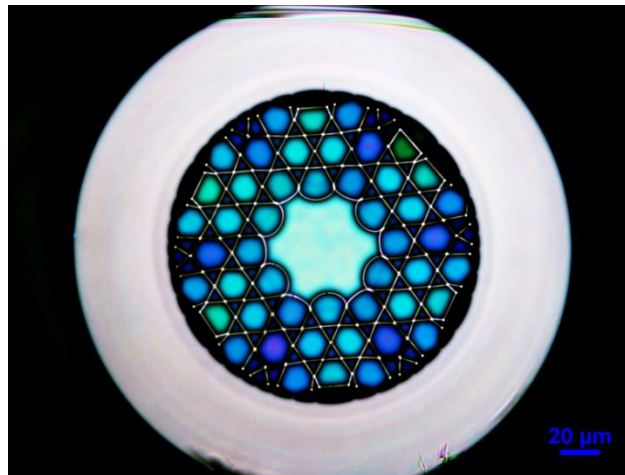
Figure 11 Microscope image of a 7-cell Kagome fibre drawn at the ORC.

The guidance mechanism in the anti-resonant fibres, has proved to be dependent mainly on the core surround thickness, thus the cladding has a limited impact on their behaviour. Thanks to this feature, it is possible to have greater flexibility in the core design compared with the case of a PBGF.

It has been demonstrated that a very little portion of the core field penetrates into the cladding [45], as it is shown in figure 12. Most of the core-cladding field overlap occurs in the core surround, thus its design can lead to improvement in the transmission of the fibre.
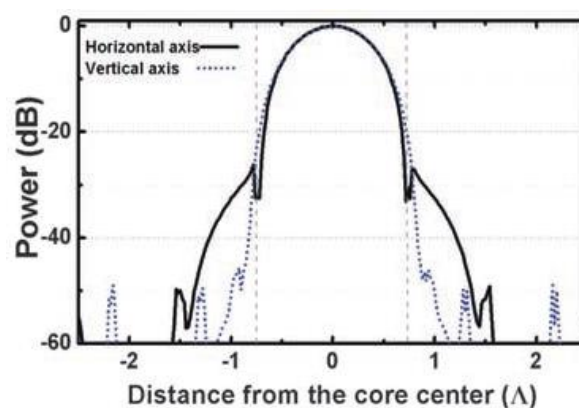
Figure 12 Confinement of the electromagnetic field in the core of a Kagome fibre [45].

24

In reference [46], Wang et al. have shown how the shape of the core surround can influence the transmission in the anti-resonant fibres. They compared the loss of two 7-cells fibres with identical cladding structure but with different shapes for the core surround. The first one has a circular core shape and an average loss ~1.4dB/m in the wavelength range 1200-1700nm. The second one has a hypocycloid, negative curvature shape of the core surround and an average loss of 0.4dB/m has been proved in the same wavelength range (figure 13).
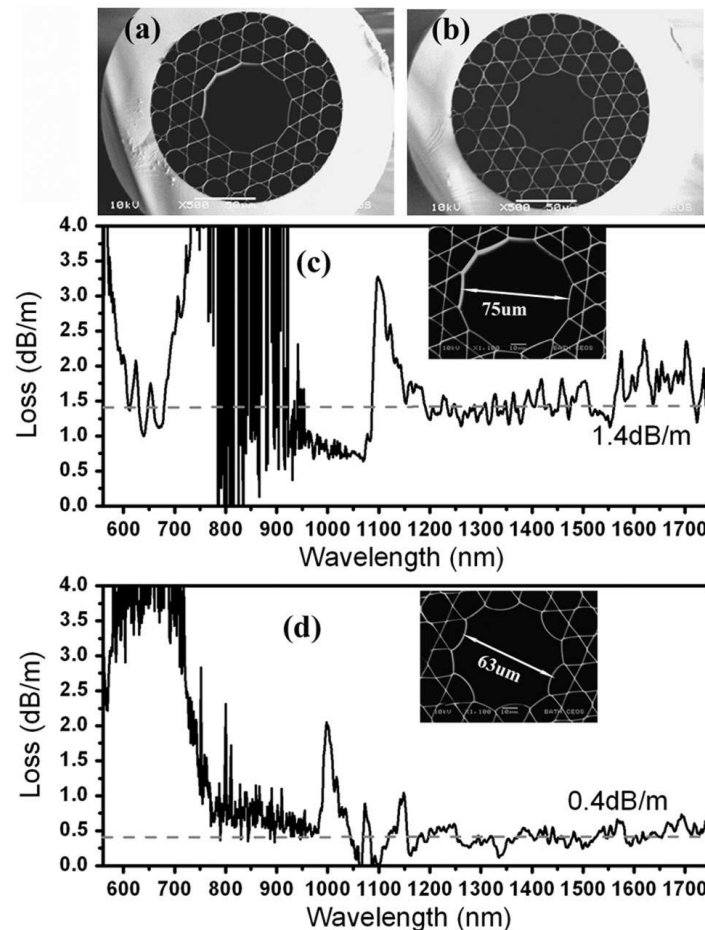
Figure 13 (a), (c) A conventional Kagome fibre with a circular core surround and its loss graph. (b), (d) the same for a Kagome with hypocycloid negative curvature core wall. [46]

Continuous research work is being done to try to optimize the shape of the core surround in anti-resonant fibres [46-48]. Particularly, the adoption of a negative-curvature core-wall leads to improvements in terms of transmission and lower losses, as shown before. In 2017, a Kagome fibre with a low loss of 7.7 dB/km at ~750 μm and lower bending sensitivity, has been fabricated by B.Debord et al. [49].

The strong dependence of the loss on the core surround, made possible to fabricate large core diameter fibres. The removal of outer hole layers, in fact, has a weak effect on the loss and, consequently, they guidance mechanism has a weak dependence on those layers [44].

Since the bandwidths of the anti-resonant fibres are not limited by the bandgap mechanism and its disadvantage (just one low loss transmission window permitted, surface modes causing

other losses etc.) and it is possible to reduce the cladding layers and obtain bigger cores, those fibres are interesting tools for gas sensing. In fact, we have more than one transmission window, and these windows are broader than the PBGF one. Let us look at figure 14, where the first high order transmission window of our Kagome and part of the fundamental one is plotted. In the enlarged detail, the pump and some gases Raman line are added to the window. The plot shows that the width of the window (~300 nm) makes possible the guidance of both the pump and the Stokes lines of the gases considered.
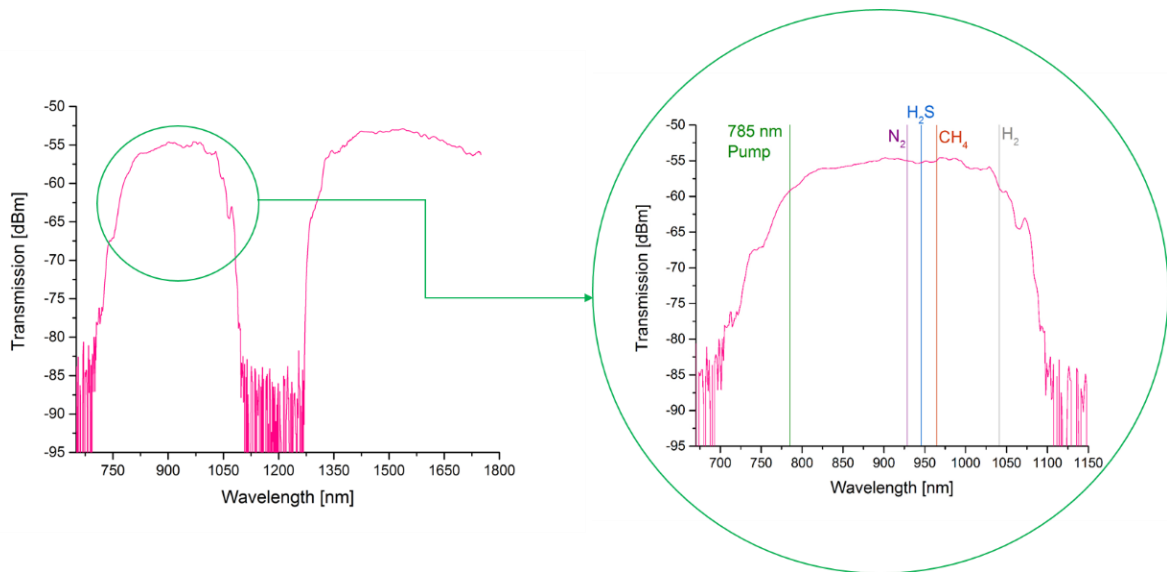
Figure 14 Left: First high transmission window of a 7-cell Kagome fibre and part of the fundamental one. Right: Detail showing the first high order window can guide the laser pump at 785 nm and the Raman wavelengths of some gases of interest.

1.6 Hollow Core Fibres for Raman gas sensing

Several research works in the past years have proved the potential of Raman gas sensing based on hollow core fibres. In 2008 Buric and al. demonstrated a ~130 times increase in the Stokes power by using an HC-PBGF rather than the traditional free space method [1]. The light from a 514.5nm laser was sent into 1.5m long section of commercial PBGF containing N_2 at ambient pressure. They used the same laser for the free space and detected both the output with a photomultiplier. In the next year, by using a different set-up arrangement, Buric and al. further improved the technique [2]. A back-scattering configuration, in which both laser input and Stokes output (backward wave) occur at the same end of the fibre, has been tested. It has been demonstrated that using PBGF in the backward configuration, the strongest Raman signal presents the lowest attenuation, while the contrary happens in forward Raman scattering [50]. With the new setup, detection of low-pressure gases in the ~ 100-ppm range has been achieved. In the same year Chen and al. detected for the first time rotational lines of Nitrogen and Oxygen by using a 1m piece of PBGF [3] and a back-forward setup configuration.

One of the most promising application for Raman gas sensing is the breath analysis. Studies have demonstrated that the presence of certain gases in an exhaled breath sample can be linked to the presence of some disease as lung cancer [51], diabetes [52] and much more. In reference [5] the researchers used 1m of a 7μm core diameter PBGF in a fibre-enhanced (backscattering) Raman spectroscopy (FERS) setup to detect the contents of a mixture of climate relevant gases and a human breath sample (figure 15). A sensitivity of 0.2 ppm for CH4 and a dynamic range of about four orders of magnitude has been achieved using 2W of a 532.2 nm laser and 20 bar of pressure.
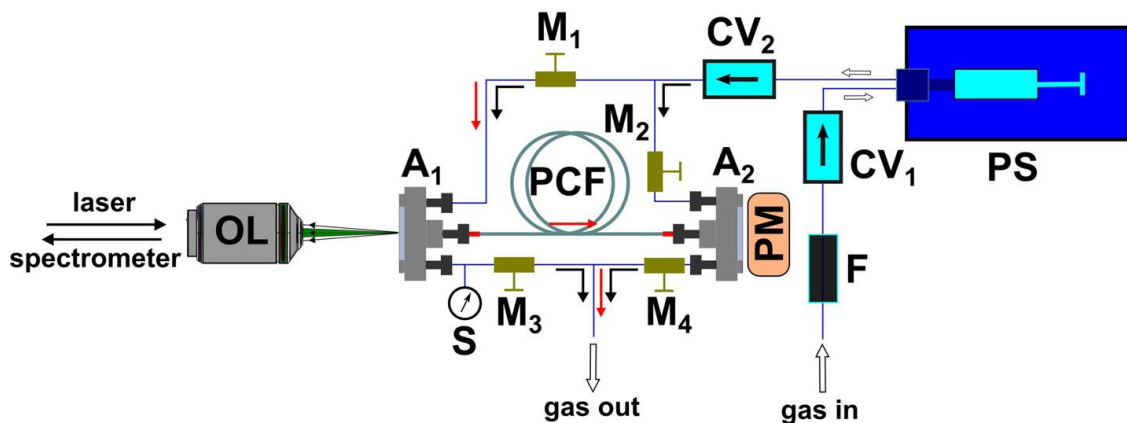
Figure 15 Setup for fibre-enhanced Raman spectroscopy (FERS) used in [5] for human breath analysis.

It has been shown that using a forward or backward configuration for Raman gas sensing with hollow core fibre, does not make a major difference if the length of the hollow core fibre is less than its attenuation length (that is the reciprocal of the attenuation coefficient) [53]. Following this principle, Chow and al, in 2014 used 2.5m of a commercial PBGF and 100 mW from a 785nm laser in a forward setup configuration. They resolved the rotational lines of pure Oxygen and pure Hydrogen at ~14bar and ~7 bar respectively. The sensitivity of their system was tested filling the fibre with ambient air at 1 bar. The Raman peaks of CO_2 were the minimum signal detectable setting a sensitivity of 15ppmv [4]. These results are interesting also for the wavelength of the source involved. Equation (10) shows that the differential scattering cross section is inversely proportional to ~ the fourth power of the laser wavelength. This is a fundamental factor to take into account when we compare results obtained in the experiments. In reference [6] a short piece of PBGF (30cm) has been used to detect gases at ~ 2 bar. Despite the fibre length was one of the shortest used in this kind of experiments, it must be considered both the 2 bar pressure and the short wavelength source they used (a laser at 532nm) contributed to obtain the Raman signal.

The Fraunhofer Institute for Physical Measurement Techniques has published the most recent paper on gas sensors based on HC-PBGFs [7]. Using 20mW of a 785nm laser and an integration time of 100s, they detected CO_2 in ambient air at one bar, proving a sensitivity of ~380ppm.

All these experiments proved the use of hollow core fibres is an advantage for Raman spectroscopy, thanks to the longer interaction length possible and to the possibility of more compact devices. Table 1 summarizes all the researches exposed in this section. From the table,

we can clearly notice that, in order to use relatively short piece of fibres, higher pressures or more powerful laser sources are required.

For the first time we report spontaneous Raman scattering from gas samples contained in a hollow core Kagome fibres and we compare the performance of this fibre with an HC-PBGF [12]. The reason we wanted to test a Kagome fibre came from the lower transmission loss it presents ~1μm compared with a PBGF fibre, moreover, those fibres have larger core diameters that, as will be exposed in 2.4.2, helps the gas filling process [54]. As we are also interested in distributed sensors (to be used for instance in the high-pressured gas pipelines) we tested longer piece of fibres (~30m) as well.

Table 1 Comparison between previous research works that used PBGF for Raman gas sensing [1-6].

References [1-6]	Fibre Type	Details	Pump Power	λ Pump	Fibre Length	Gas used	Pressure	Sensitivity	Detection
Buric, AO, 2008, A	HC-PBGF	HC-580-01 from NKT	45 mW	514.5 nm	1.5 m	N_2	1 ATM		0.55m focal length grating spectrometer+EMI 9789A PTM in photon counting mode
Buric, AO, 2008, B	HC-PBGF	HC-580-01 from NKT	< 1 W	514.5 nm	1.5 m	Natural gases (Methane, ethane, and propane)	High pressure		JY IHR550 Spectrometer (SPEC) and an EMI 9789A phototube (PMT).
Buric, AO, 2009	HC-PBGF	HC-580-01 from NKT	100 mW	514.5 nm	1 m	Ambient air (N_2, O_2), natural gas or syngas		20 ppm for Ethane and Propane	0.55m grating spectrometer+PMT or IR CCD
Chen, SPIE, 2009	HC-PBGF	HC-580-01 from NKT		514 nm	100 cm and 59 cm	N_2, O_2	1 ATM		Spectrograph+CCD
Chow, MP, 2014	HC-PBGF	HC-800-01 from NKT	100 mW	785 nm	2.5 m	Pure oxygen gas, Pure Hydrogen gas, 5% CO_2 balanced with N_2	~13,8 ATM, 6,8 ATM, 1 ATM	~15 ppmv of CO_2 @ 1 ATM	Low noise 100 × 1340 pixel, liquid nitrogen-cooled, backilluminated, deep depletion, near-IR optimized CCD camera
Hanf, ACS, 2014	HC-PBGF	HC580-02 from NKT	2 W	532.2 nm	1m	CO_2, CH_4, and N_2O together with N_2, O_2	up to ~20 ATM	0.2 ppm for Methane @ ~20 ATM	Spectrometer: Acton 2556 with LN2-cooled back-illuminated CCD detector
Jochum, RSC, 2016	HC-PBGF	HC-PCF (NKT)		532 nm	30 cm	O_2, CO_2, NH_3 and C_2H_4	~2 ATM	20% O_2, 500 ppm CO_2 and 250 ppm C_2H_4 (remainder N_2).	Spectrometer: Acton SP2500, Princeton Instruments, grating with 1800 lines

2 Setup Design

2.1 Introduction

In this chapter, the setup rig will be described in detail: every component choice will be discussed together with an explanation of the mode of operation and the methods used to post-treat the Raman signals acquired. Furthermore, in 2.4.2, the equations describing the Raman scattering from gases contained in hollow core fibres will be described.
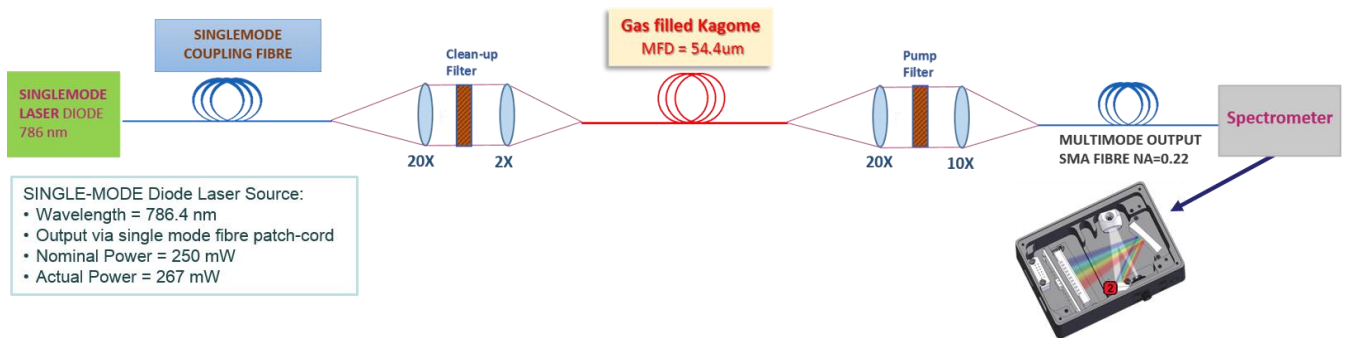
Figure 16 Detailed Setup Scheme

The experimental set up used to test the Kagome fibre is shown in Figure 16. The laser diode is a Lumics 784.6 nm single mode laser, pigtailed with a single mode fibre (SMF) patchcord. The light from the SMF is coupled into the Kagome with an arrangement of two objective lenses (20X and 2X) to "adapt" the mode field diameter (MFD) of the single mode patchcord to the MFD of the Kagome fibre. A clean-up filter is placed in front of the first lens to have a clean laser line. Previous measurements of the laser spectrum had showed it presents a wide bandwidth pedestal that extends in the wavelength range of the Raman lines and cannot be removed by the pump filter (figure 17).
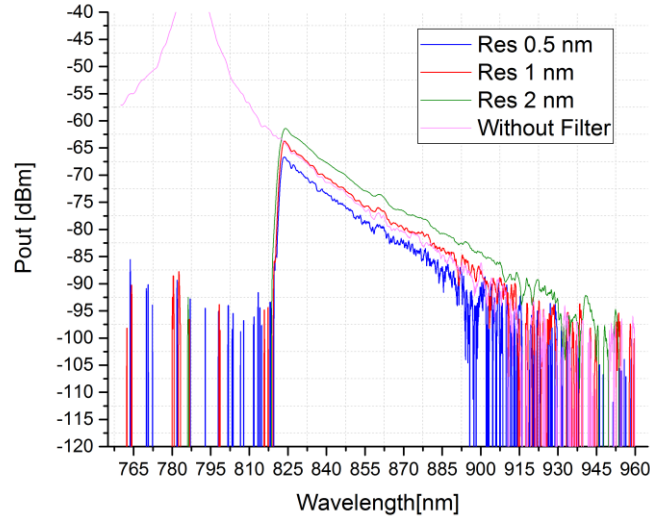
Figure 17 Spectrum of the laser diode at 786.4nm with and without the pump filter. The measurement has been done with an optical spectrum analyser at three wavelength resolution values.

At the output of the Kagome fibre, the light is coupled into a multimode (MM) fibre (connected to the spectrometer) through another arrangement of objective lenses (20X and 10X). To remove the laser line and obtain just the Raman lines from the gas into the Kagome, a pump filter has been inserted between the last two lenses. Another pump filter is inside the spectrometer to have a better filtering and to avoid any damage to the CCD of the spectrometer.

Reaching an optimal alignment of the laser beam into the hollow core fibre is fundamental to have a good coupling efficiency and transfer as much power as possible.

As shown in figure 16, the light beam coming from the SMF pigtail of the laser is coupled into the Kagome through an arrangement of two objective lenses, 20X and 2X respectively. Through the lenses, the mode field diameter of the SMF (4.6 μm) is "enlarged" to better match the MFD of the Kagome (~41 μm).

Ideally it should be:

$$\frac{f_2}{f_1} = \frac{MFD_{Kagome}}{MFD_{SMF}} \cong 9 \quad (13)$$

Where f_1 and f_2 are the focal length of the two objective lenses.

In reality, the focal length ratio is ~ 6.4, as the first lens in front of the patchcord (20X) has f_1=8.33 mm and the lens that focus the beam into the Kagome (2X) has f_2 = 53mm.

The first lens is used to collimate the beam and to enlarge its MFD (or its beam waist, $w_0 = MFD_{SMF}/2$).

Considering that:

$$w(z = f_1) = w_0 \sqrt{1 + \left(\frac{z}{z_R}\right)^2} \approx w_0 \frac{f_1}{z_R} \quad (14)$$

where $z_R = \frac{\pi w_0^2}{\lambda}$ is the Rayleigh length.

30

From the Gaussian beam theory, at the output of the first lens, the beam waist will be:

$$w_{0,1} = \frac{\lambda f_1}{w_0 \pi} = \frac{786.4 \times 8.33mm}{(4.6\mu m/2) \times \pi} = 0.9mm \qquad (15)$$

A black board has been placed at ~1m of distance from the first lens, to check the collimation of the beam. The laser light was then focused by the second lens into the Kagome obtaining a beam waist size at the 2X lens focal length of:

$$w_{0,2} = \frac{\lambda f_2}{w_0 \pi} = \frac{786.4 \times 53mm}{w_{0,1} \times \pi} \cong 14.74\mu m \qquad (16)$$

Then the output of the Kagome has been tested with the thermal head of a power meter (PM). To optimize the output power, we aligned the Kagome with the X and Y axes of the movable stage where it sits, but we also had to adjust the distance from the second lens in order to have as much power transmission as possible. This means that the actual focal length of the second lens (53mm) might not be the optimal distance to have the best MFD match between the SMF and the Kagome (and so the maximum output power possible). As calculated before, the beam spot size produced at the focal length has a diameter of 14.74*2 µm, while the Kagome MFD is ~ 41 µm. Moving the Z-axes of the movable stage, we adjusted the distance of the fibre from the 2X objective lens to read the maximum output power possible on the power meter. Ideally, if we can exactly match the size of the beam entering the Kagome with its MFD, we will excite mainly the fundamental mode, thus we could have high power transmission at the output. This means that the distance between the tip of the fibre and the 2X lens, should not be the focal length where the beam size is ~12 µm less than the MFD of the Kagome.

After the optimization of the Kagome output, a similar arrangement of lenses has been used to collimate and refocus the beam into the MMF that goes to the spectrometer. In this case, the two fibre (Kagome and MMF) have similar core dimension of ~50 µm. We did the same collimation and alignment procedure explained for the first stage (SMF, 20X and 2X lens and Kagome) also for this output stage (Kagome, 20X and 10X lens and MMF) using the PM.

2.2 The Laser source

The choice of the laser source for Raman spectroscopy was challenging as it was necessary to find a "trade-off" between several options. Equations (9) and (10) in chapter 1 show Raman Stokes intensity depends on the fourth power of the frequency so that an UV source looks like the best choice. However, UV sources are expensive, the optics should be chosen carefully because of the high-energy radiation and, more important, many gas species absorb in the UV. Several research works on Raman gas sensing used sources in the visible range of the light spectrum [1], [2, 3], [5], [6]. However, as the setup would also have been tested with a PBGF, the attenuation of this kind of fibres has a λ^{-3} lower limit dependence due to surface scattering loss (see for instance reference [55]). Therefore, another source to consider was a NIR (near-infrared) laser like an Nd: YAG (Neodymium YAG) laser at 1064nm.

The trade-off we chose to meet both the requests for stronger Raman intensity and lower attenuation of the fibres, has been a single mode laser diode at 786.4nm, which is also a relatively cheap device. In the first version of the setup, a multimode 785 nm laser source has also been tested, but the excitation of the higher order modes of the fibres, lossier than the fundamental one, caused the loss of ~97% of transmitted power. The single mode laser instead has proved an output on input power ratio of ~45% with 27m of Kagome fibre.

2.3 Spectrometer

A diffractive spectrometer constitutes the detection stage of the setup. The light exiting the last MMF (figure 16) is collimated by a collimating mirror and sent to a fixed diffraction grating that diffracts the incoming light at different angle depending on the wavelength. All of the different-wavelength beams are then focused on a CCD array by a focusing mirror (figure 18). The CCD is an Andor iVac cooled Silicon detector with an array of 1650 x 200 pixels of 16μmx16μm size. Thanks to the cooling, the dark noise, due to the thermal excitation of electrons, is as low as 0.0028 e⁻/pixel/second.
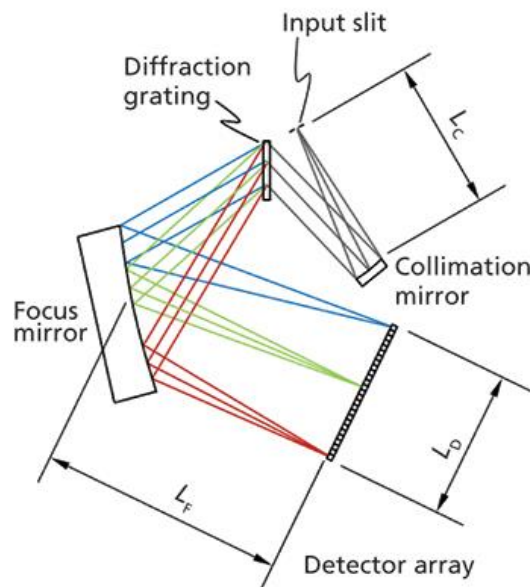
Figure 18 Scheme of a dispersive spectrometer (spectrograph) [56].

Sections 2.3.1 and 2.3.2 will discuss the calibration of the spectrometer and the post-processing of the spectra acquired (through the flat field correction). Paragraph 2.3.3 contains an explanation of the noise sources that should be considered using a CCD.

2.3.1 Calibration

The CCD inside the spectrometer is composed of 1650 x 200 pixels, each receiving a specific wavelength from the grating (depending on the angle that wavelength is transmitted). The photons arriving on the pixels are converted into electrons and then in data we can actually read and analyse thanks to an interface software developed by my industrial sponsor Is Instruments. Each detected spectrum is saved as a matrix: number of counts versus pixel number. In order to associate each pixel to the corresponding wavelength (or wavenumber) value, it is necessary to calibrate the spectrometer. This means a calibration standard must be used; here we used the well-known position of the peaks of a Xenon lamp spectrum plus the position of Nitrogen and Oxygen Raman lines from ambient air.

The calibration has been done in four steps:

1. Localization of four peaks of the Xenon lamp spectrum in pixels on the spectrometer (figure 19).
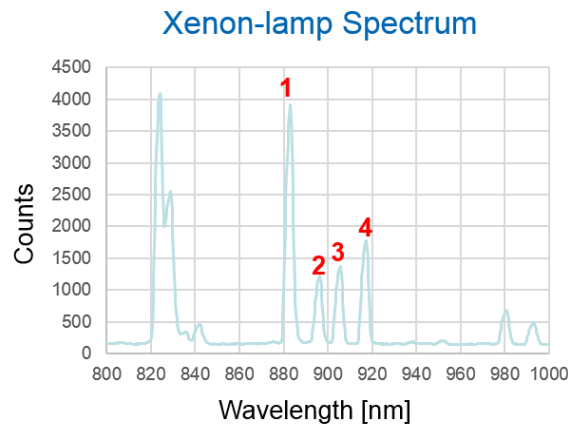
Figure 19 Xenon-lamp spectrum, the peaks indicated by the red numbers are been used for the calibraiton of the spectrometer.

2. Localization of Nitrogen and Oxygen Raman lines in pixel on the spectrometer using the ambient air contained in the hollow core fibre.

3. Plot of wavelengths versus pixels with the theoretical values of the peak wavelengths (λ_t) of the Xenon lamp and Nitrogen and Oxygen Raman lines and the pixels value obtained in 2 and 3

4. Fitting with a third order polynomial (figure 20) to find three coefficients (c_i) and an intercept (I) to obtain which wavelength corresponds to a specific pixel.

$$\lambda(pixel) = I + c_1 p_1 + c_2 p_2^2 + c_3 p_3^3 \qquad (17)$$

The coefficients and the intercept of the fitting have then been used as parameters to obtain calibrated wavelength axes in the computed data.
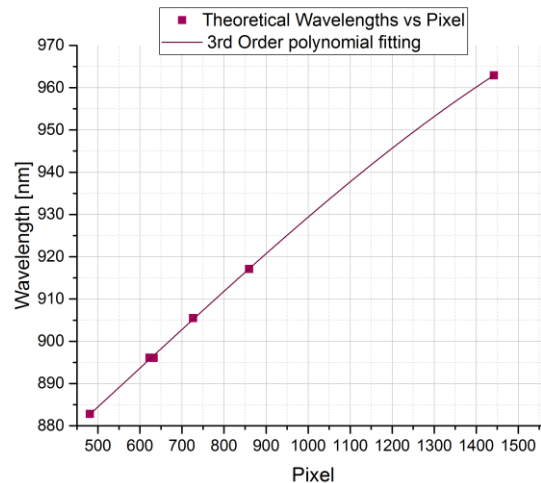
Figure 20 Theoretical Raman wavelengths versus experimental pixel values corresponding to the four Xe-lamp peaks plus the N$_2$ and O$_2$ peaks. The figure also shows the polynomial fitting of the points.

2.3.2 Flat field correction (FFC)

When the CCD is shone with a white light source, the intensity versus pixel response does not look flat and the oscillations can go from 0.1% to 10%. Considering for instance two adjacent pixels, "1" and "2", the sensitivity difference between them can go from 0.1% to 1%.

This effect is due to the product of several factors:

- Quantum efficiency of the detector (DQE). This is the efficiency of the detector (the CCD) in converting photons in electrons. The higher the quantum efficiency, the higher is the sensitivity of the detector. Since the sensitivity of the detector change with the wavelength (the CCD is made of Silicon, more sensitive in the range 400-700nm), the DQE is described by a curve.
- Degrading reflectivity, due to the degradation of the reflecting layers of the mirrors in the spectrometers.
- Optical Efficiency. It affects the sensitivity as well and is wavelength-dependant. This quantity depends on the specific geometry of the photodetector, (the Silicon in the case of the CCD) and the other components of the pixels structure (size and shape of the aperture of the pixel and of the photodetector itself, and length of the dielectric tunnel) [57].
- Filters used in the setup not having a flat response in the wavelength range of interest.

To correct the difference in sensitivity of the pixels of the CCD, every spectrum detected by the spectrometer must be divided by the so-called "flat field correction vector" (FFC), but first, it is necessary to subtract the dark spectrum to each measurement. The dark spectrum is the spectrum acquired when all the light sources are turned off and is due to the noise (read noise and dark current) and the bias voltage of the instruments and does not dependent on the pixel-to-pixel sensitivity.

The FFC has been obtained by collecting and summing 102 measurements of the spectrum of the white light source (flat spectrum) and 102 measurements of the dark spectrum in order to

have good statistics. The sum of the dark spectrums vector must be subtracted from the flat field vector and divided by the mean value of the subtracted vector to finally obtain FFC:

$$FFC = \frac{\sum_i FlatFieldSpectrum - \sum_i DarkSpectrum}{mean(\sum_i FlatFieldSpectrum - \sum_i DarkSpectrum)} \qquad (18)$$

The integration time for each acquired spectrum was set to obtain ~1million counts in each pixel. The reason is that the error is proportional to the square root of the number of counts, thus, to have 0.1% error, we need 1 million counts.

Every spectrum acquired with the spectrometer has been post-processed applying the flat field correction to consider the non-uniform pixel-by-pixel sensitivity of the CCD:

$$S_c = \frac{Measured\ Spectrum}{FFC} \qquad (19)$$

where S_c is the corrected spectrum.

2.3.3 Noise of the CCD

The spectrum measured by a CCD, depends on the number of photons arriving on the pixels, the quantum efficiency (as explained in 2.3.2) and the integration time, i.e. the total time the CCD will collect the light arriving on it.

In order to obtain the signal to noise ratio (SNR) three fundamental noise components have to be considered: the shot noise, the dark noise and the readout noise. Each of them is independent from the other. Shot noise is an intrinsic noise of the CCD. It is due to the statistical variation of the rate of arrival of the photons on the pixels. The uncertainty in the measurements of the number of photons collected in a specific time interval follows the Poisson statistic. Shot noise is the ultimate noise limit of the CCD, meaning that is the minimum level of noise achievable, and is proportional to $\sqrt{S}$, where S is the signal. Dark noise is caused by the dark current, this is the thermic-generation rate of electrons at a specific temperature of the CCD. If the CCD is cooled, like in our spectrometer, this contribution is negligible. Finally, readout-noise is due to the electronic of the CCD, i.e. the process of converting the generated electrons in a voltage signal, process them and apply the analog-to-digital conversion. This kind of noise is the same for all the pixels and it is usually generated by the output amplifier of the CCD. In some CCDs the noise of the amplifier depends on the frequency used to read the single frame [58]. In our CCD we can reduce the readout noise using the minimum readout speed (in Hertz), equal to 35 KHz.

Considering all these noises, the SNR is:

$$SNR = \frac{S/FFC}{\sqrt{\frac{S + N_{BG}}{FFC} + N_{DC} + N_r^2}} \qquad (20)$$

where:

- S = detected spectrum (number of counts collected in the integration time interval)
- N_{BG} = counts due to residual light in the ambient and not to the signal source, they produce their own shot noise, so it must be added to the total noise.
- N_{DC} = Dark noise (negligible in our cooled CCD)
- N_r = Root mean square (rms) of the Readout noise.

2.4 The "gas cell"

As discussed in the previous sections, a hollow core fibre is used to contain the gas under test in these experiments. The use of a fibre as gas cell, allows longer interaction lengths with the laser light which is simultaneously guided in the hollow core while occupying a minimum of space compared with the free-space arrangement in which the gas is usually contained in a bulky glass box.

In section 1.5, it has been shown how using a Kagome fibre might be advantageous for Raman gas sensing compare to the use of a PBGF. Broader bandwidths make the guidance of both the laser wavelength and the Raman lines possible and greater flexibility in the core design than in the PBGF leads to the possibility of larger cores and therefore fast gas filling. However, the Kagomé and PBGFs are multimode fibres and the excitation of those high order modes causes loss in the transmitted power. Nonetheless, as it will be explained in the next paragraph for an anti-resonant Kagome fibre, optimizing the coupling of the laser beam MFD with that of the fundamental mode, improves the power transmission.

The loss of the fibre is another important aspect to consider in the analysis of the results as the fundamental equation of the Raman theory itself must be modified to take account of the wavelength-dependent loss evolution (see paragraph 2.4.2).

2.4.1 High Order Modes (HOM) and the importance of the launch conditions

High Order Modes in anti-resonant Kagome fibres have higher confinement and bend loss as compared to the fundamental mode. Therefore, the excitation of those modes, leads to power loss. With the small spot size of the laser beam we obtain with the lens and fibres arrangement of the setup (see 2.1), we are more likely to excite these modes just slightly changing the launch condition and thus moving the spot from the centre of the core.

Dr Bradley and colleagues used three different launch conditions to understand how these conditions affect the excitation of the modes in a 7-cells anti-resonant Kagome fibre (ARF Kagome) [59]. The light was launched in the fibre through a single mode fibre (SMF-28) with ~10.4 μm MFD (at 1550nm), an endlessly single mode fibre with ~26 μm MFD and, finally, a free space lens arrangement, from the SMF to the ARF, that produced a focused spot size of ~58 μm. The differential group delay plots in figure 21 show that a greater number of higher order modes are excited when the light was butt-coupled into the Kagome through the single modes fibres compared to the case in which the light was coupled inside the ARF with the lens arrangement. This last launch conditions provided also the most symmetric and central

excitation of the fundamental mode. In the worst case, this is launching with the SMF-28 which has the smallest MFD, LP02-like modes were mostly excited. Those modes present an intense central lobe with a Gaussian profile. For this reason, they can be confused with the fundamental mode. The large mode field diameter mismatch between the Kagome and the SMF should most likely represent the reason of the excitation of HOM.

Therefore, a good matching of the Kagome MFD with the MFD produced by the launch stage is very important in terms of modal content and in order not to excite too many HOM, the MFD of the beam launched in the Kagome, should be as close as possible to the MFD of the fundamental mode of the Kagome itself.
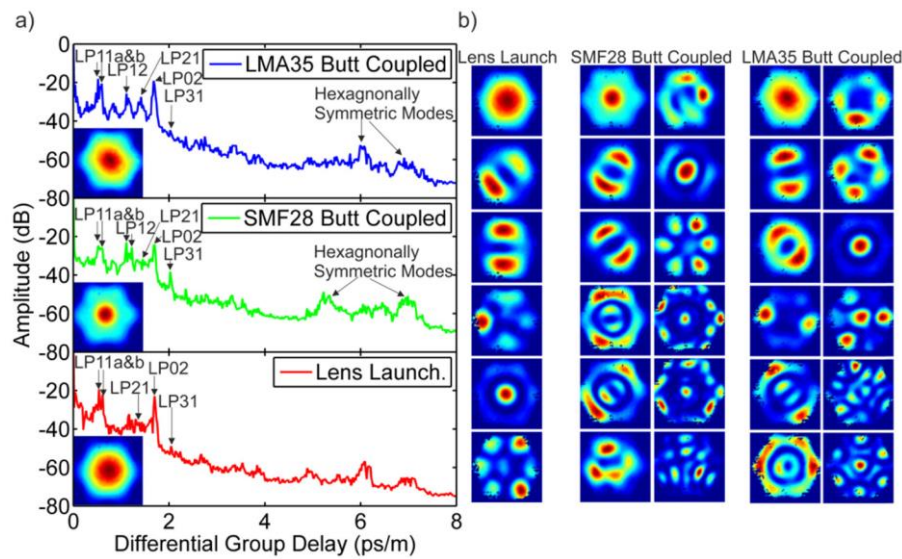
Figure 21 a) DGD curves for free space lens launch (red), butt coupling with SMF-28 (green) and LMA-35 (blue) through 21 m of 7 cell Kagome. Inset: beam profiles summed over all wavelengths for each launch condition. b) S2 mode profiles for the three different coupling conditions [59].

2.4.2 Properties of the fibres

The Raman Stokes power equation in chapter 1, does not consider that the transmission loss of the fibre is wavelength-dependent.

To measure the transmission loss of the hollow core fibres used as gas cell in the experiments, the so-called "cutback technique" has been adopted. The result for the Kagome is shown in figure 22: the pink trace in the graph represents the loss of the fibre in dB/km. The graph shows also four straight lines at Nitrogen, Oxygen and Carbon Dioxide Raman wavelengths, plus an orange straight line at the pump wavelength. The transmission loss value almost doubles from 786.4nm (wavelength of the laser source) to the Oxygen wavelength (896.04nm) and reaches ~170dB/Km at $\lambda = 962.91$nm, where the Nitrogen Stokes line sits. It is necessary to take those different values of loss into account when we apply the Raman Stokes formula to calculate the output Raman power expected from the gas sensor.
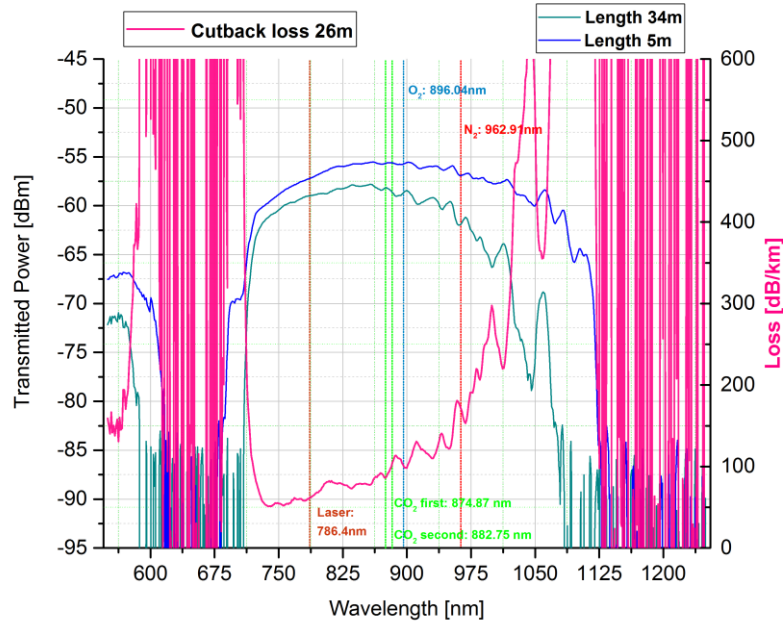
Figure 22 Cutback measurement for the 7-cells Kagome fibre used in the setup. The straight lines indicate the wavelengths of the Raman lines for Nitrogen (red), Oxygen (blue) and Carbon Dioxide (green) with a laser source of 786.4nm (orange straight line).

Figure 23 shows the loss spectrum of the hollow core PBGF used in the experiments obtained using the cutback technique from 284m to 10m. The loss at the pump wavelength and at the Oxygen Stokes wavelength is ~170 dB/km and 110dB/km respectively. Due to the very high attenuation, the loss at the Nitrogen Stoke wavelength has been estimated to be ~500 dB/km using shorter piece of fibre. As discussed in 1.4, an HC-PBGF transmit with the lower attenuation over a single spectral window, but, the abrupt interruption of the periodic cladding causes the so-called surface modes localized within this transmission window. The impact of those modes on the transmission can be noticed in figure 41 at wavelengths around 870nm and 960nm.
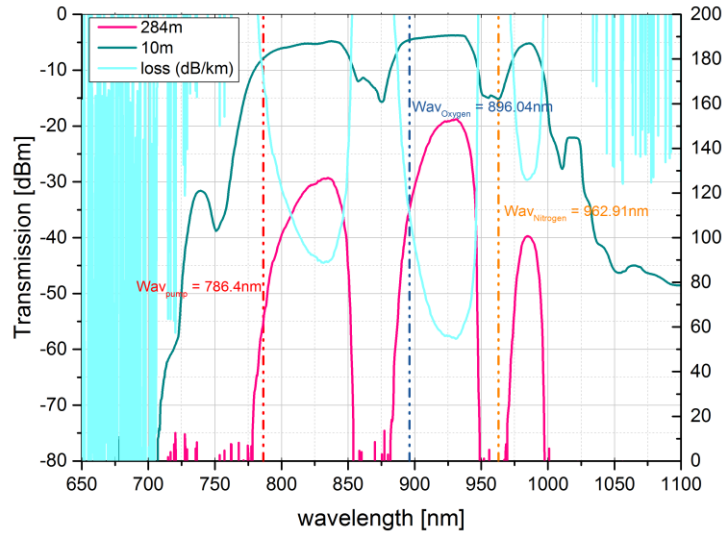
Figure 23 Cutback transmission and loss measurements on the hollow core photonic bandgap fibre used in the experiments.

To consider the loss of the hollow core fibres and its impact on the Raman intensity, let us consider equation (10) from chapter 1, expressing it in terms of power instead of intensity:

$$P_S = kP_L \rho L \left(\frac{\partial \sigma}{\partial \Omega}\right) \Omega \quad (21)$$

To consider the impact of the different losses for every Raman wavelength, we should modify the equation [9]:

$$P_{Stokes} = kP_{Pump} \times \left(\frac{\partial \sigma}{\partial \Omega}\right) \times \rho \times \Omega \times e^{-\alpha_R L} \times \left[e^{(\alpha_R - \alpha_P)L} - 1\right] \times \frac{1}{(\alpha_R - \alpha_P)} \quad (22)$$

Where:

α_P = loss at the pump wavelength

α_R = loss at the Raman wavelength

If we consider a point x along the fibre length, the Raman power generated in that point will be:

$$dP_{Stokes}(x) = \sigma P_{Pump} \times e^{-\alpha_P x} \quad (23)$$

where $\sigma = k \left(\frac{\partial \sigma}{\partial \Omega}\right) \times \rho \times \Omega.$

Because in that point the pump power is:

$$dP(x) = P_{Pump} \times e^{-\alpha_P x} \quad (24)$$

Therefore, at the end of the fibre we will have:

$$dP_{Stokes,out}(x) = \sigma P_{Pump} \times e^{-\alpha_P x} \times e^{-\alpha_R(L-x)} \quad (25)$$

For the Stokes power generated in x.

Integrating over all the length of the fibre, we obtain the expression of equation (22). If the loss at the pump and that at the Stokes wavelengths are the same, equation (22) simplifies to the equation (21) times $e^{-\alpha_R x}$. Besides, if the transmission loss is negligible (like in the traditional free space setups for Raman gas sensing), we find again the linear dependence of Raman power on the interaction length L as expressed in equation (21).

Figure 24 shows the results of Matlab simulations for four different loss values, considering the Kagome and ~78% of Nitrogen inside the fibre (Nitrogen concentration in ambient air) and the 786.4nm pump:

1. 170dB/km of loss at N_2 wavelength (962.91nm) and 33dB/km for the pump wavelength
2. 5dB/km of loss for both N_2 and pump wavelengths
3. 10dB/km of loss for both N_2 and pump wavelengths
4. 33dB/km of loss for both N_2 and pump wavelengths.
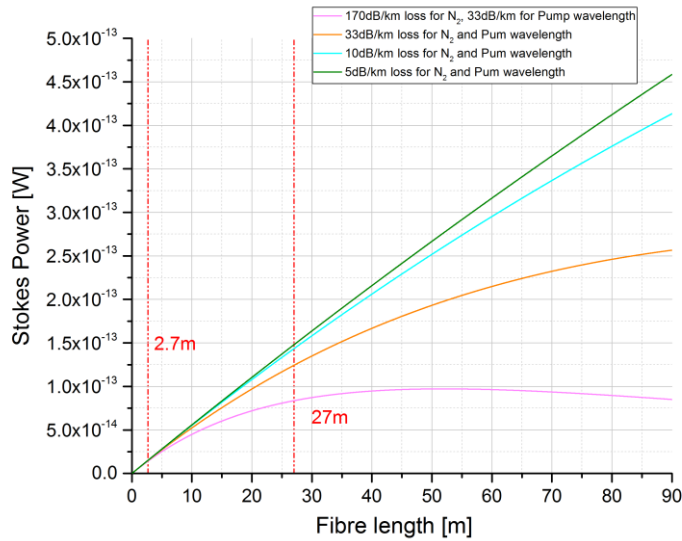
Figure 24 Stoke power of Nitrogen at ambient pressure vs fibre length. Four different cases have been considered. The red trace represents the actual fibre used in the setup, with a loss of ~33dB/km for the laser pump and ~170dB/km for the Nitrogen Raman line. The green, blue and orange traces are simulations for hypothetical 5, 10 and 33 dB/km loss values for both Nitrogen Raman and pump wavelengths. The two straight lines indicate the length points of 2.7m and 27m fibre lengths.

The first case depicts the transmission loss of the Kagome fibre used in the setup (pink trace on figure 24), where the loss at the pump wavelength is more than five times lower than the loss at the Nitrogen Raman wavelength (33dB/km vs 170dB/km). In this situation, the graph shows how the Stokes power remains linear with the fibre length only for small values of the length itself. This observation will be important for the analysis of the data presented in the next section. Furthermore, the simulations show there is an optimal value for the fibre length

to have a stronger Stokes signal. Picture 25 shows that, after ~50m, increasing the length of the Kagome is not useful; while theoretically it should improve the Raman power (equation (10) in chapter 1), increasing the length over a certain value, causes the Stokes power to decrease due the no more linear connection between power and length.
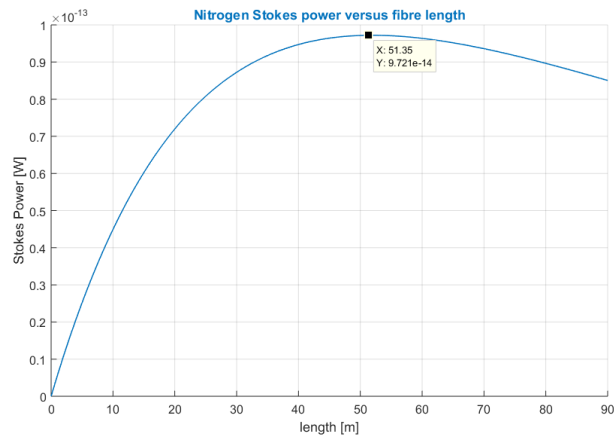
Figure 25 Ambient air Nitrogen Stokes power vs Kagome length. Using a fibre longer than ~50m fibre causes the Raman power to decrease.

Another important aspect must be pointed out in equation (21), the solid angle observed Ω in the equation is considered as function of the numerical aperture NA of the fibres [1]:

$$\Omega \propto (\sin^{-1} NA)^2 \qquad (26)$$

Digonnet and al. in reference [60], proposes an analogy with the conventional fibres showing how the acceptance region is still a solid cone (figure 26) but this cone is frequency dependent causing the acceptance angle and therefore the NA to be frequency dependant as well.
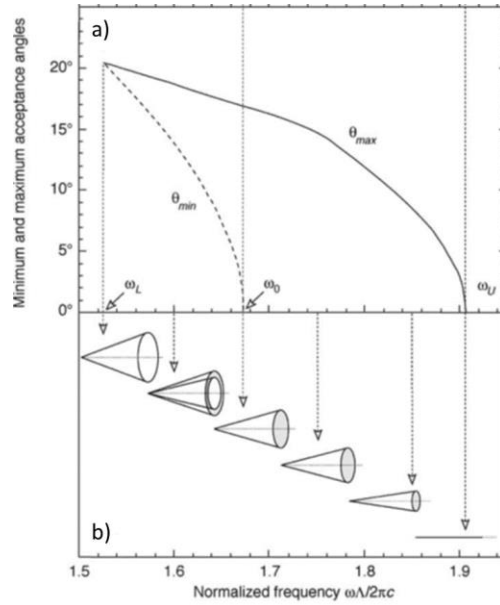
Figure 26(a) Frequency dependence of the maximum and minimum acceptance fibre. (b) Evolution of the solid angle with the frequency [60].

The numerical aperture of the Kagome fibre has been roughly calculated in the lab to measuring the divergence of the laser beam out of the fibre. Several beam spots have been taken at increasing distance from the fibre end with a CCD camera. Then the pictures acquired have been computed with Matlab to measure the full-width-half-maximum (FWHM) of the intensity profile for each length. Knowing the evolution of the FWHM with the distance, it was possible to achieve the acceptance angle and therefore the numerical aperture of the fibre (~0.023). For the PBGF, instead, the NA has been assumed ~0.12 from calculation found in literature [60]. Table 2 summarises all the property of the two type of HC-PFC discussed in this section.

Table 2 Comparison of the parameters of the two hollow core fibres

Fibres Comparison	PBGF	Kagome
Loss @ Pump λ = 786.4nm [dB/km]	170	33
Loss @ CO_2 λ (both peaks) [dB/km]	TOO HIGH	~75
Loss @ O_2 λ = 896.04nm [dB/km]	110	100
Loss @ N_2 λ = 962.91nm [dB/km]	~500	170
Numerical Aperture (NA)	~0.13	~0.023
Core Size [μm]	16	~50

The core size, also reported in table 2, is another important parameter to accelerate the gas filling of the fibre, as demonstrated in reference [54] by Dicaire and al. Based on the theory equations of this paper, some simulation have been run to predict the gas filling time for the Kagome fibre, which has a core size of 54μm. The simulations plots (figure 27 and 28) will

show also the strong dependence of the filling time on the pressure of the gas we want to flush into the fibre.

Figure 27 shows the results of the Matlab simulations for the filling time versus length (1m to 29m) of our Kagome fibre, supposing we are filling the fibre with 7 and 20 bar of Nitrogen (1bar = 10^5 Pascal). Those values have been chosen because, as it will be shown in the experimental part, the Kagome has been filled with a mixture of Nitrogen and CO_2 (1%) increasing the pressure from 1 to 7 bar. The gas chambers we are using for the experiments and the gas regulators on the gas bottles are currently tested to support 20 bar, tops. As shown on figure 27, increasing the pressure of ~2.2 times (from 7 to 20 bar), we reduce the filling time for a 29m piece of Kagome, of more than 2.7 times (from 5 to 1.8 minutes).
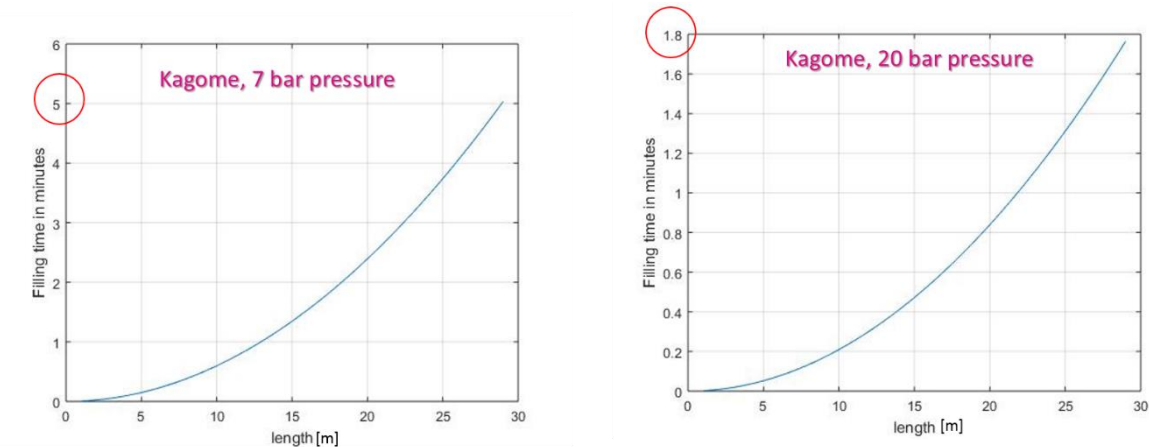
Figure 27 Filling time versus Kagome fibre length supposing to flush the fibre with 7bar Nitrogen (left) and 20bar Nitrogen (right). As shown, the filling time decreases of ~2.7times increasing the gas pressure from 7 to 20 bar.

Figure 28 shows the simulations when the pressure increases from 1 to 90 bar for both lengths. Even though currently we have not the right instrumentations to try our fibre with 90 bar, this is one of the aim of the project. The gas in the pipelines where the sensor would be used, in fact, is pressurized at 90 bar.

From the plots in figure 28, is evident how increasing the pressure has also a strong impact on the filling time. With 90 bar, even 29m of fibre can be filled with Nitrogen in less than half minute. Furthermore, considering increasing the pressure of just 4 bar (from 1bar, ambient pressure, to 5 bar) the filling time decreases quickly (of ~7 times in the 29m length case, of ~8 times for the 1m piece).

All the theory and the formulas used in the simulations, can be found in reference [54].
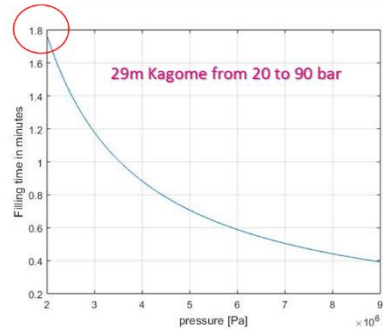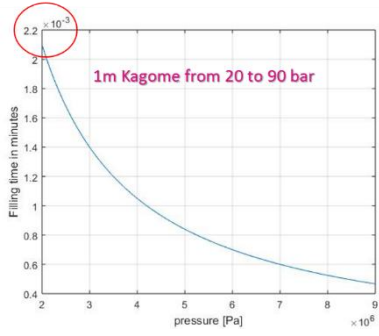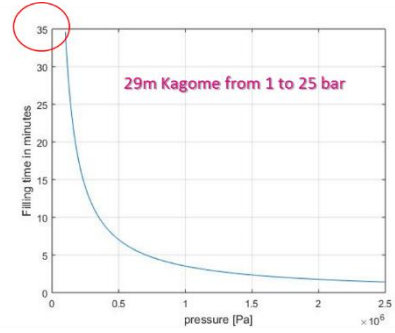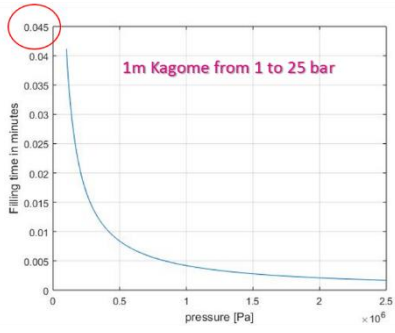
Figure 28 Filling time for 1 and 29m Kagome supposing to flushing the Kagome fibre with Nitrogen and increasing the pressure from 1 to 90 bar.

3 Experimental Result

3.1 Measurement preparation and procedure

Once the HC-PCF had been carefully aligned within the experimental set up described in 2.1, we could start to collect measurements of the Raman Stokes signals. In these experiments, as we were planning to compare the performance of two different fibres as a function of pump laser power, knowledge of the power coupled into the HC-PCF for each recorded spectrum was essential. For every recorded spectrum, we first checked the input power (power recorded after the laser clean up filter) and the output power (power exiting the third lens, after the Kagome fibre) using a power meter. This meant that for each measurement we could calculate the coupled power into the HC-PCF through knowledge of the fibre attenuation. By doing this, we made sure to have repeatable and reliable measurement all the times.

3.2 Acquired spectra and post processing

The first experiments have been run using the Kagome fibre described in 2.4 for which we achieved an input coupling efficiency of ~90% and an output over input ratio of ~45% for 27m of fibre.

An integration time (or exposure time) of 60 seconds has been set on the CCD for most of the measurements. Since the level of noise would increase with the integration time as well, was important to choose a trade-off to obtain a good signal level and an acceptable level of noise that would had made the detection of weak signal possible, like CO_2 in ambient air. Carbon dioxide represents, in fact, just the 0.03% of the ambient air.

Initial tests on 27m of Kagome, showed a slightly out of focus and not perfectly calibrated spectrometer as shown in figure 29, where the strength of the Raman signal is expressed in number of photons detected (counts). The theoretical wavelength values for Nitrogen, Oxygen and Carbon Dioxide with a pump of 786.4nm are:

- CO_2: 874.87nm ($2\nu_2$) and 882.75nm (ν_1)
- O_2: 896.04nm
- N_2: 962.91nm
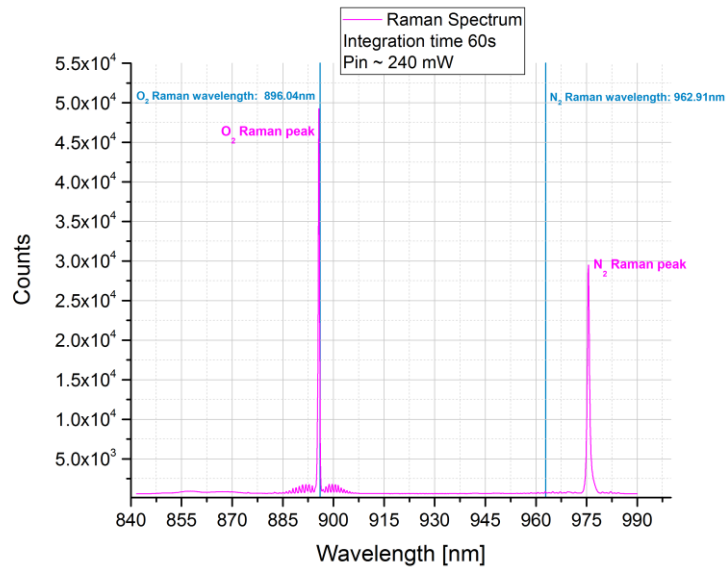
Figure 29 Raman spectrum of ambient air in the Kagome without subtraction of background spectrum and FFC. The Spectrometer not perfectly calibrated, causes the Raman lines not to sit in the exact theoretical position (blue straight lines).

When the spectrometer is perfectly calibrated, the Raman peaks should sit exactly at those values. Furthermore, the figure shows, especially for Nitrogen, a broader and not perfectly symmetric Raman line than the one expected. This effect is due to the focusing of the spectrometer.

The figure shows also that the Nitrogen peak is lower than the Oxygen one. Since the scattering cross section ratio between O_2 and N_2 is ~1.3-1.4 and their concentration ratio in ambient air is ~0.27, one expects to see a higher Nitrogen peak compared with the Oxygen one.

To correct this effect, the flat field correction must be applied, as already explained in section 2.3.2.

After the re-calibration and re-focusing of the instrument by IS Instruments, new Raman spectra have been acquired. Before the analysis of the results, a set of post-processing has been applied to every spectrum:

1. Subtraction of the background trace previously acquired by blocking the laser light after every measurement (see 3.3).
2. Flat field correction.
3. Subtraction of a noise baseline (user defined) to calculate the actual number of counts under the Raman peaks for each measurement

The result of this set of corrections is shown in figure 30. In the right graph, the Nitrogen peak is higher than the Oxygen, as one can expect from the scattering cross section and gas concentration ratios. A more precise analysis, based on the actual number of counts for the two Raman lines, will be done in section 3.5, as we should consider the width of the peaks to do a suitable comparison between the Raman Stokes powers of the gases contained in the fibre.
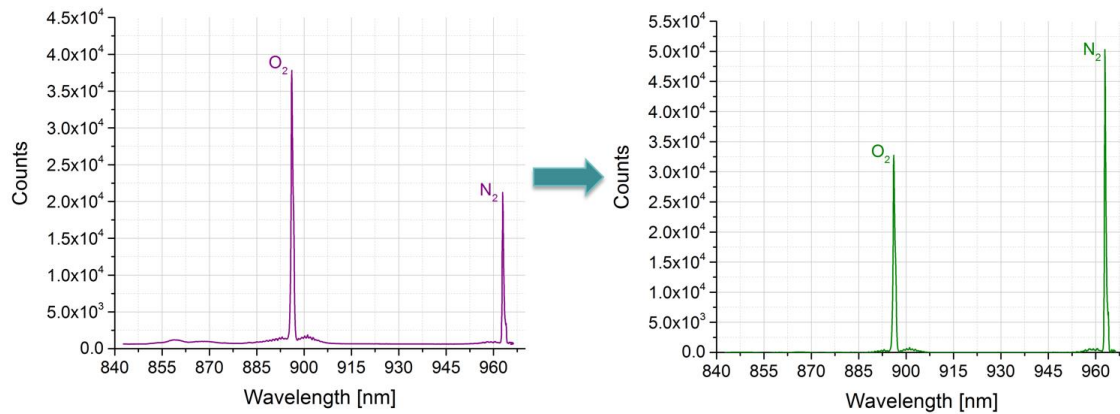
Figure 30 Detected Raman spectrum before (purple) and after (green) all the corrections: subtraction of the background noise and flat field correction. The right graph shows a higher Raman signal for Nitrogen, as predicted by the much higher concentration of the gas in ambient air compared to the Oxygen.

3.3 Silica Raman noise

We run the first set of experiments using 27m of Kagome fibre filled with ambient air at ambient pressure. We set an integration time of 60s to acquire the Raman spectrum of the gases with the spectrometer and run a set of measurements changing the power of the laser source. For each measurement, we also acquired the dark spectrum blocking the laser beam and measuring just the photons arriving on the detector from the room light.

A small amount of power travels in the solid silica cladding around the core and can generate a Raman signal, which reduced the signal to noise ratio (SNR). Around 850-875nm in the plot of figure 31, we can observe two bumps; they are silica Raman noise and they grow with the power (entering the fibre) as predicted by the Raman theory (left plot). To minimize this noise, it is important to optimize the launch conditions, this is the alignment of the fibre and the beam spot size. The right graph of figure 31 shows the effect of the misalignment of the fibre. The experiment has been done systematically moving one of the axes of the movable stage, on which the Kagome sits, from 0μm to 14μm. As we can see, the alignment is important to reduce the effect of the silica noise.

This effect could be corrected by a background subtraction. Evacuating all the gas inside the fibre (with a vacuum pump) it is possible to collect just the counts coming from the silica Raman. This reference background can be subtracted to every future measurement to optimize the SNR. Another simple way to remove it, could be a background subtraction using a baseline, as silica Raman is a weak, broadband effect (~20nm) with a short Raman shift (around 1000 cm^{-1}), so easily distinguishable from the gas lines.
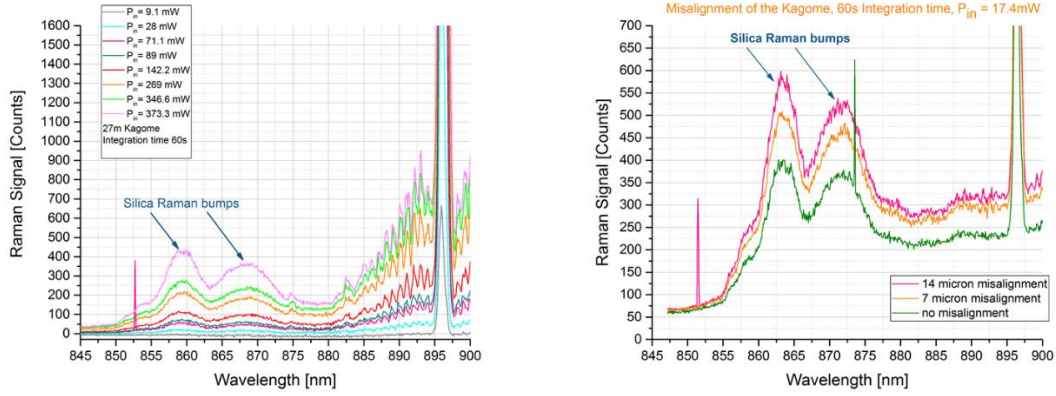
Figure 31 27m Kagome fibre, Silica Raman noise growing with power (left) and by misaligning the fibre (right).

3.4 Results and Analysis

Raman theory predicts that the Stokes power is proportional to the scattering cross section and to the concentration of the analyte gas, so, theoretically, the ratio between the Nitrogen Raman Stokes and the Oxygen one should be:

$$\frac{P_{N_{2,R}}}{P_{O_{2,R}}} = \frac{\sigma_{N_2} \times c_{N_2}}{\sigma_{O_2} \times c_{O_2}} \cong 2.76 \quad (27)$$

Where:

- σ_{N2} = scattering cross section of Nitrogen = 1
- σ_{O2} = scattering cross section of Oxygen ≈ 1.3-1.4
- c_{N2}= Nitrogen concentration in ambient air = 78.09%
- c_{O2} = Oxygen concentration in ambient air = 20.95%

This means the Nitrogen Stoke should be ~2.7 times strongest than the Oxygen one. Figure 32 shows the results are in good match with this theoretical value. The figure depicts the growing of the sum of the detected power (in number of counts detected by the CCD) under the Raman peak for N_2 and O_2 versus input power into the Kagome. We can observe this growth agrees with the linear connection between Raman power and input power of the theory. Considering the linear fitting for both the set of data, we can calculate the ratio of the slope to compare it with the theoretical ratio value of 2.7. The result for the data shown in figure (32) is ~2.7, equal to the expected value.
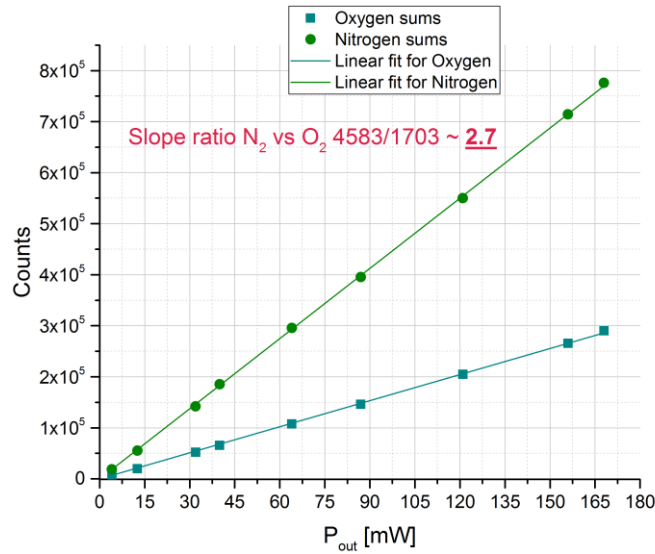
Figure 32 Sum of the counts under the Raman peaks for Oxygen (blue) and Nitrogen (green) with linear fitting vs power exiting the 27m fibre (~45% the input power). The slope ratio of the two linear fittings is ~2.7, equal to the theoretical value.

Figure 33 shows three output Raman spectra for the ambient air contained in the hollow core fibre. The first on the left corresponds to a detected power out of the Kagome of ~4.1mW, a value almost corresponding to the laser threshold. The plot in the middle shows how, with an output power of 64mW (~15.6 times stronger than the previous case), the number of counts of the peaks increases proportionally. Same in the last trace on the right, corresponding to an output power of 168mW (max power coming from the laser source).
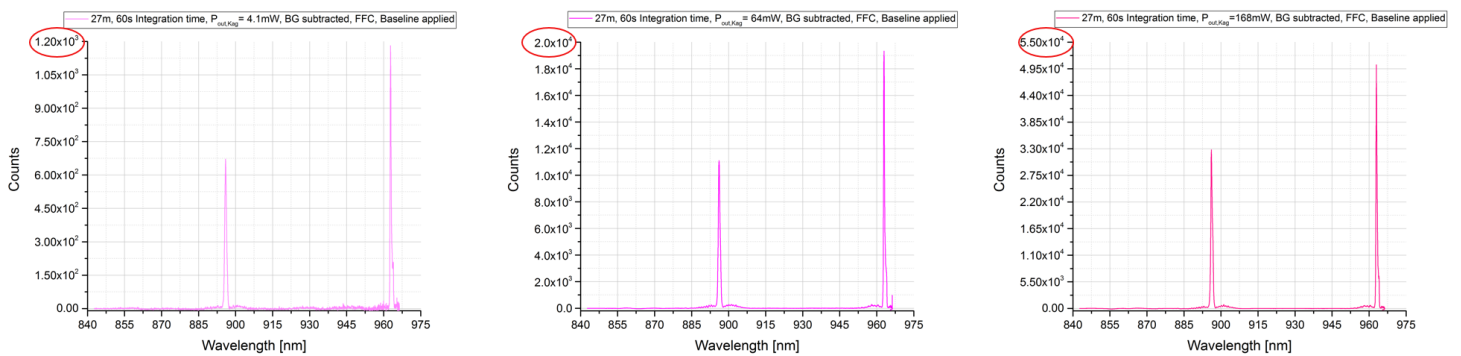
Figure 33 Comparison of the output Raman spectrum detected by the spectrometer for three different power level exiting Kagome fibre (~45% the input power): 4.1mW (left), 64mW (centre) and 168mW (right).

The same set of measurements has been run for a 2.7m piece of Kagome fibre. Figure 34 shows the sum of counts under the Raman peaks of O_2 and N_2 vs input power. As in the case of the long piece of Kagome, the slope ratio of the linear fittings for the two gases is in good agreement with the theoretical value.
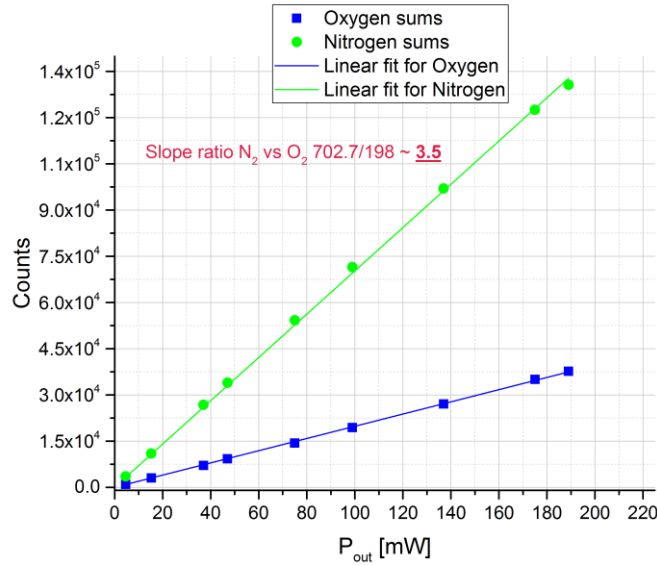
Figure 34 Sum of the counts under the Raman peaks for Oxygen (blue) and Nitrogen (green) with linear fitting vs power exiting the 2.7m fibre (~90% the input power). The slope ratio of the two linear fittings is ~3.5, in good agreement with the theoretical value.

It is also important to compare the results for the different lengths of Kagome. From the theory, we expect the Raman Stokes power to grow linearly also with the length of the interaction path between the gas and the light, i.e. the length of the fibre in our case. We would expect a ~10 time stronger Raman signal changing from a 2.7m Kagome to a 27m one. However, the experiments gave different results for both Nitrogen and Oxygen (see figure 35). The increase in signal for Oxygen and Nitrogen, from a 2.7m Kagome to a 27m one, is respectively ~7.6 and ~5.7.
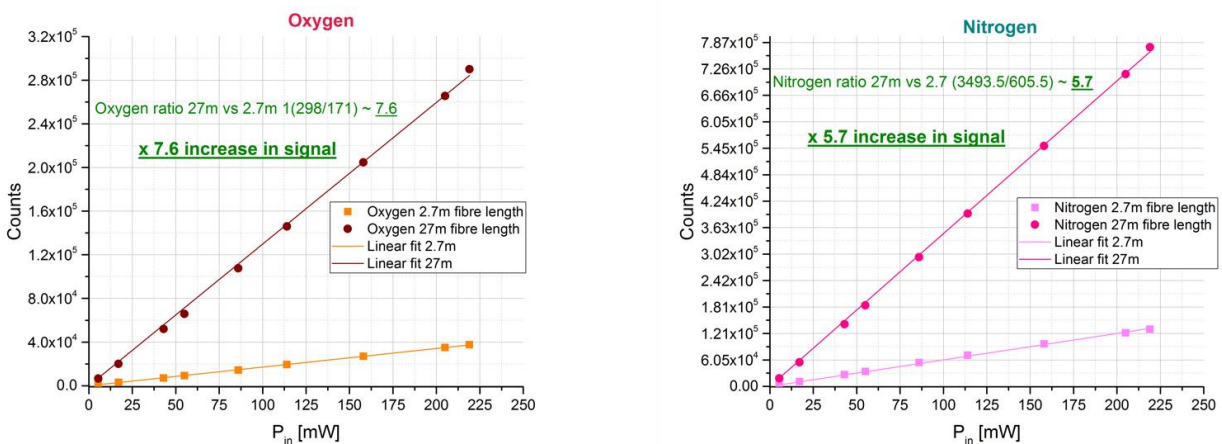
Figure 35 Growth of the Raman signal with power for Nitrogen and Oxygen considering two different lengths of Kagome fibre: 2.7m and 27m. The Stokes signals are linear with the input power but not with the fibre length as expected from the theory. The different transmission loss (in dB/km,) for the Raman wavelengths of the two gases, causes the non-linear behaviour.

As explained in paragraph 2.4.2, the loss of the fibre is strongly wavelength-dependent. Therefore, at the different Raman wavelengths of N_2 and O_2, the loss of the Kagome fibre will have a different impact on the output Stokes power. From the cutback measurements on the fibre used in the setup, the losses at the Raman wavelengths for the gases are:

- ~100 dB/km @ O_2 Raman wavelength
- ~170dB/Km @ N_2 Raman wavelength

Therefore, is important to consider the impact of the fibre loss when using a longer piece of Kagome. As already explained in paragraph 2.4.2, the Stokes signal will not be linear with the fibre length. The graph in figure 36 is the result of the simulation to calculate the theoretical Stokes power for different gases (considering the equation (22) in paragraph 2.4.2). From the simulations, the ratio between the Stokes power obtained in 27m and 2.7m of Kagome fibre should be less than 10:

- ~7 for Oxygen
- ~5.8 for Nitrogen

Those theoretical results explain why the experimental growth of the Raman power with the fibre length cannot be linear with the length of the fibre.
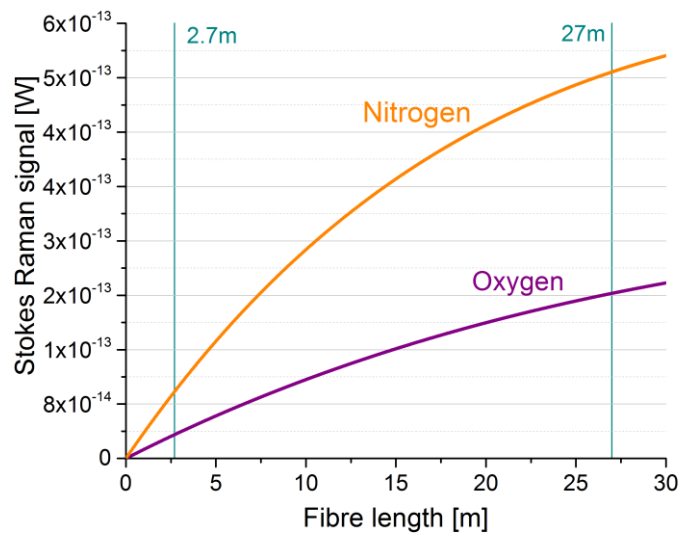
Figure 36 Non-linear growth of the Stokes signal with the Kagome fibre length due to the strong wavelength-dependence of the transmission loss. The straight lines indicate the two fibre lengths used in the experiments (Matlab simulations).

3.5 Rotational lines and CO_2 in ambient air at ambient pressure

Carbon dioxide in ambient air has a low concentration of around 380ppm (~0.04%). Figure 37 shows the detected spectrum of the ambient air inside 27m of Kagome fibre, with an integration time of 60s and the laser set at maximum power. In the detail on the right, we can observe the two Raman peaks of CO_2 (874.87nm and 882.75nm) and some of the rotational Raman lines of O_2 (right end side of the graph).
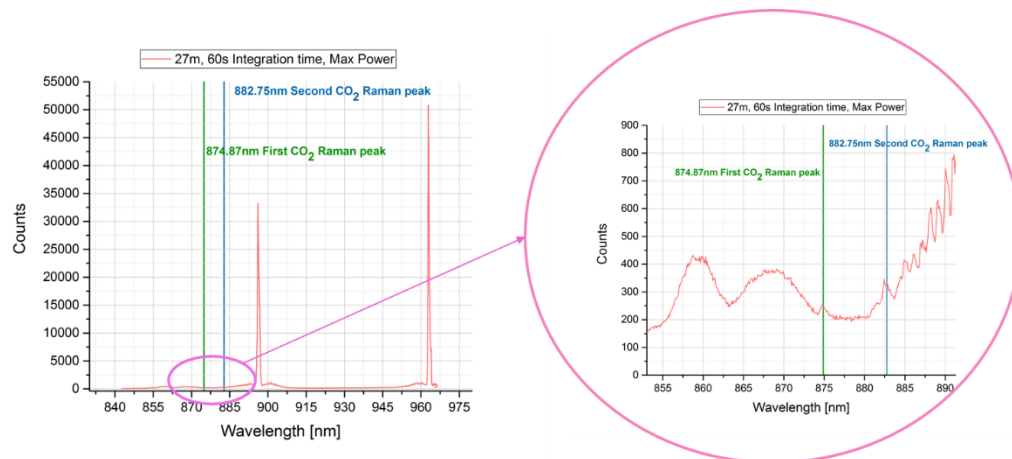
Figure 37 Detected spectrum of the ambient air contained in the Kagome after 60s of exposure time and the laser set at maximum power. The detail in the circle shows the two peaks of CO_2 and, on the right end side, some of the rotational lines of O_2.

Figure 38 shows the results of a set of measurements done by increasing the power into the fibre from a value close to the laser threshold to the maximum. The coupled power in the Kagome, considering an output on input ratio of ~45%, are shown in the legend on the left. The plot shows the second Raman peak of CO_2 starts to be visible from P_{in} ~70mW. The first, weaker peak can be observed at a slightly higher power (~40mW). The figure shows also the rotational lines of the Oxygen starting from an input power of ~28mW.

Raman gas sensing, as already explained in chapter 1, is a weak effect. The small Stokes powers are mainly due to the low values of scattering cross section in gases. If we consider the low concentration of the carbon dioxide in ambient air and the fact we were working at 1atm, catching the CO_2 peaks is a proof of the project success. With the current set up, we proved a detection capability of some hundreds of ppms and a dynamic range that goes from the Nitrogen concentration of 78%, to the small 0.04% of CO_2.
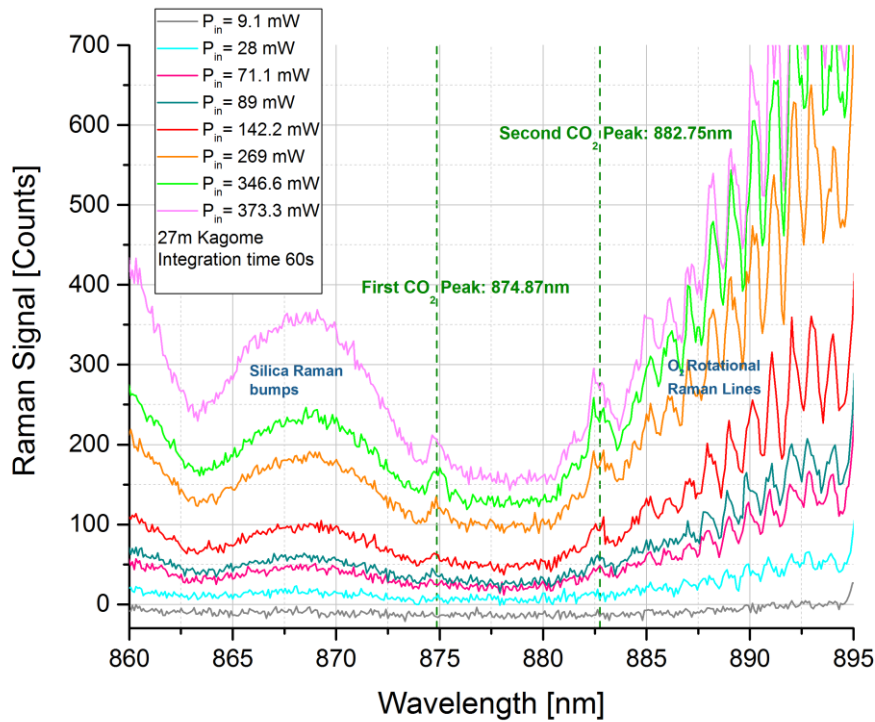
Figure 38 Detail of the detected spectrums of the air contained in the Kagome increasing the power entering the fibre. The plot shows the two peak of CO_2 can be detected with a minumum input value of ~70mW. On the right end side (between 885 and 895nm), also the rotational lines of O_2 can be observed from an input power value of ~28mW.

3.6 First high-pressure measurements

Developing a gas sensor that can be used in high-pressure environments (like a gas pipeline, up to 90bar of pressure), is one of the goal of this project. Therefore, we modified the setup to use it with high-pressure gases.

The first measurements have been done with a gas bottle containing Nitrogen plus a 1% of CO_2 and the pressure has been changed from 1bar (ambient pressure), to a maximum pressure of 7bar.

3.6.1 High-pressure setup and chambers

First, we had to find a way to pump the gas into the Kagome fibre. It means both the ends of the fibre had to be linked to the bottle containing the gas we want to flush in, and isolated from the external ambient. Here at ORC, fibre gas chambers for vacuum experiments had already been used. We adapted the design of those chambers to use them with high-pressure gases. Figure 39 shows the Kagome fibre inserted in one of these high-pressure chambers through a fibre holder.
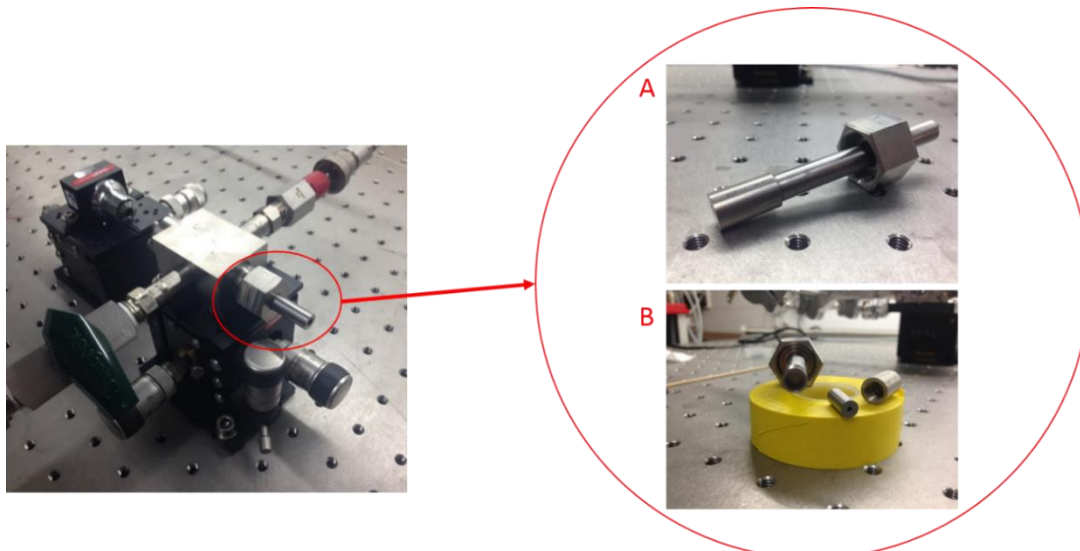
Figure 39 A high-pressure chamber used in the setup. The fibre is connected through a fibre holder shown in the detail on the right. A) Assembled fibre holder, B) the fibre holder disassembled.

On the opposite side of the fibre holder, the chambers have a thick glass window that permits the light from the fibre to reach the third lens of the setup.

Another perspective of the gas chamber mounted on the movable stage is shown in figure 40; in the detail is shown the front of the chamber with the glass window. On the right side of the chamber, a quick connector is used to connect the chamber to the hose going to the gas bottle. On the right side, a gauge is connected to the system to check the pressure inside the chamber (and the Kagome).
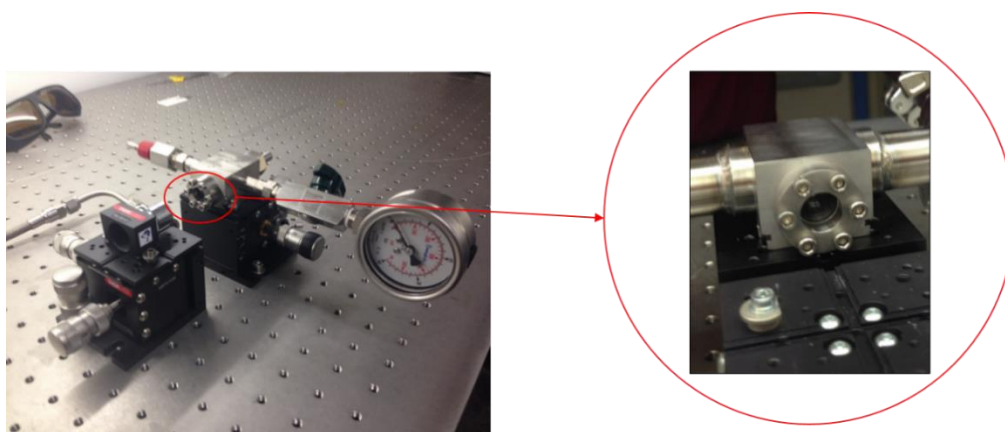
Figure 40 Left: The high-pressure gas chamber sitting on one of the movable stage of the setup. A gas gauge is connected on the right side of the chamber and a quick connector (opposite side) will connect the system to the gas bottle. Detail on the right: the front of the gas chamber showing the glass window that permits the light to exit the chamber.

The other end of the Kagome has been connected to an identical chamber to have an isolated system.

The current setup can support up to 20 bars of pressure. Unfortunately, in our first set of measurements, we could use just one chamber, since the other one had a leak problem (now fully resolved). However, the current configuration can simulate a real on-field environment, with one end of the hollow core fibre exposed to the environment under test. Moreover, initial

test of the setup, showed that the pressure remains constant into the Kagome for long enough to run the measurement with the pressure we set from the bottle (figure 41).
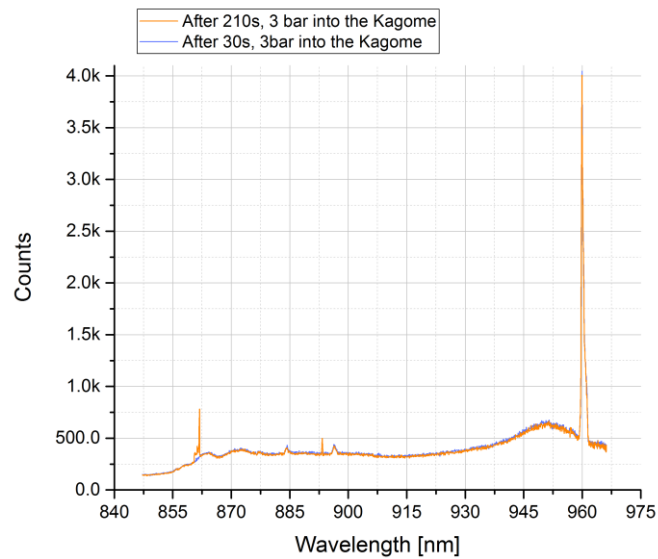
Figure 41 Maintaining a constant pressure of 3 bar, we kept flushing the fibre with N_2 + 1% CO_2. Not big differences in the spectrum after ~210 seconds, made the measurement at a single pressure value, possible even with one end of the Kagome exposed to the external ambient.

3.6.2 Results and analysis

When we started the high-pressure measurements, the Kagome fibre was filled with ambient air. To purge the fibre, we start flushing gas from a bottle containing N_2 and 1% of CO_2 setting a pressure of 3 bar using the regulator on the gas bottle.

The first spectra have been recorded 8, 8.5 and 12 minutes after the purging started. As already shown in figure 41, the spectrum did not change with time when the pressure was kept constant (the pressure value has been checked on the gauge attached to the chamber). Figure 41 shows two small peaks around 885nm and 890 nm and a high peak at the Nitrogen Raman wavelength (~960nm). The two small peaks correspond respectively to CO_2 and O_2. The presence of O_2 inside the fibre, proved that some ambient air was still contained into the Kagome. However, the small number of counts for the Oxygen Raman peak shows the ambient air was being purged by the gas mixture from the bottle flushed inside the fibre.

Then, the pressure has been increased from 3 bar to 7 bar. At each pressure point, we recorded the spectrum in different moments, to check the pressure remained constant into the fibre. Figure 42 shows a detail of the detected spectrum at 2, 3, 4, 5 and 7 bars (unfortunately, the file of the measurement at 6 bars was corrupted). While increasing the pressure, more and more gas from the bottle was flushed into the fibre while the ambient air (and so the Oxygen) was purged away.
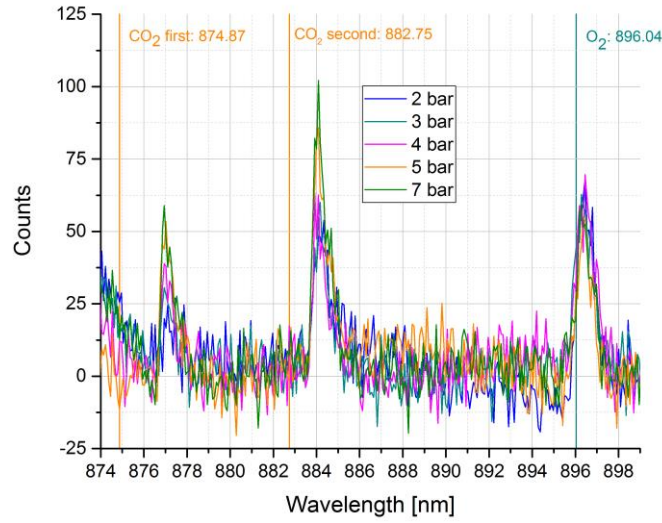
Figure 42 Detail of three Raman spectrums of the gas contained into the Kagome. A mixture of N_2 and CO_2 (1%) was flushed into the fibre. The measurements have been done increasing the gas pressure from 2 to 7 bar. While the ambient air was purged out of the Kagome (amount of O_2 in the fibre decreasing), the CO_2 Raman peaks grew with the pressure as predicted by the Raman theory. Due to the not perfect calibration of the spectrometer, the actual Raman lines appear slightly shifted towards higher wavelengths than the theoretical wavelength values.

To check the accuracy of the measurements for the weak peaks of CO_2, the signal to noise ratio has been considered (see 2.3.3 in chapter 2). The higher the SNR, the more accurate can be the measurement. The uncertainty is given by 1/SNR, so considering a minimum SNR of 10, with an uncertainty greater than 10%, the signal is too weak compared to the noise to be distinguished from it. Shot noise has been considered for these high-pressure measurements. It is caused by the light coming from the fibre and the residual ambient light that the CCD detect and is equal to:

$$N_{TOT} = \sqrt{(S + N_{BG})/FFC} \qquad (28)$$

Where S is the signal and N_{BG} is the background noise (from the ambient). FFC is the flat field vector used to correct the measurements as explained in 2.3.2.
The SNR is then equal to:

$$SNR = \frac{(S - N_{BG})/FFC}{\sqrt{(S + N_{BG})/FFC}} \qquad (29)$$

As for the ambient pressure experiments, the counts under the Raman peaks have been summed to observe the behaviour of the Stokes power (in number of counts) when the pressure increases. Before the sum, a baseline has been subtracted to the spectra to take into account the actual counts under the peaks without noise pedestals. The minimum and maximum wavelengths considered to sum the counts under the first CO_2 peak are:

1. $\lambda_{1,CO2}$ = 876.52 nm
2. $\lambda_{2,CO2}$ = 877.94 nm

while for Nitrogen:

1. $\lambda_{1,N2} = 985.81$ nm
2. $\lambda_{2,N2} = 961.85$ nm

Table 3 summarizes the SNR and the uncertainty δ of the measurements at the central wavelength of the range used where the counts under the Raman peaks of CO_2 (first peak) and N_2 have been summed. The table shows that the measurements for Nitrogen have low uncertainty, while the SNR for the first detections of the CO_2 is low if we consider a minimum SNR of 10. In figure 43, we can observe the growth of the CO_2 peak with the pressure and the relative error bars for each point. To add the error bars, the uncertainty in the range of wavelengths ($\lambda_{1, N2}$ - $\lambda_{2, N2}$) and ($\lambda_{1, CO2}$ - $\lambda_{2, CO2}$), is supposed to be almost constant and equal, for each pressure point, to that quoted in table 1. For instance, at 2 bar, the uncertainty would be 10.2%.

Table 3 SNR and uncertainty (δ) at each pressure point for CO_2 (first peak) and N_2.

CO2 (first peak)	2 bar	3 bar	4 bar	5 bar	7 bar
(Signal-Noise)/FFC	363.125	349.676	392.713	350.572	384.643
Noise in λc	37.12	36.9	37.5	36.9	37.4
SNR	9.8	9.5	10.4	9.5	10.3
1/SNR=δ	10.20%	10.56%	9.55%	10.50%	9.72%
Nitrogen	2 bar	3 bar	4 bar	5 bar	7 bar
(Signal-Noise)/FFC	1790.66	2313.8	2605.3	3006.12	3662
Noise in λc	68.1	71.8	73.8	76.5	80.6
SNR	26.3	32.2	35.3	39.3	45.4
1/SNR=δ	3.80%	3.11%	2.83%	2.54%	2.20%
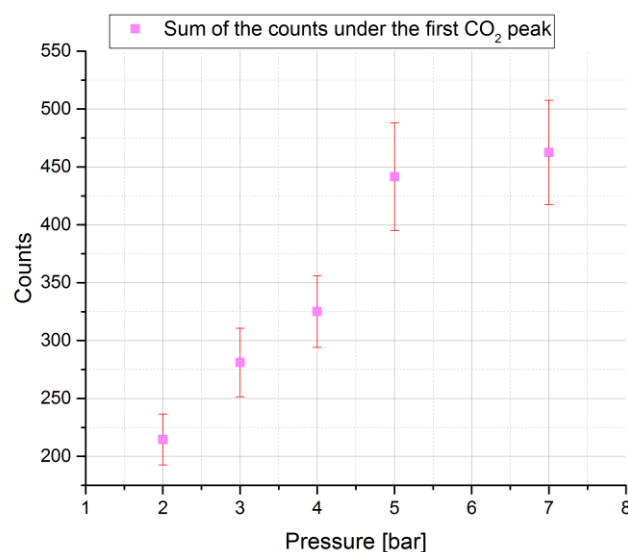
Figure 43 Growth of the first Raman peak of CO2 with error bars. The uncertainties in the measurement are the ones listed in table 2.

Figure 44 a) shows the increase of the Nitrogen peak with pressure. The plot in figure 44 b) shows sum of the counts under the N_2 peak versus pressure with its linear fitting and error bars. The growth of the N_2 peak is well described by the linear fitting, so it agrees with the Raman theory that predicts a liner dependence of the Stokes power on pressure.

a

b
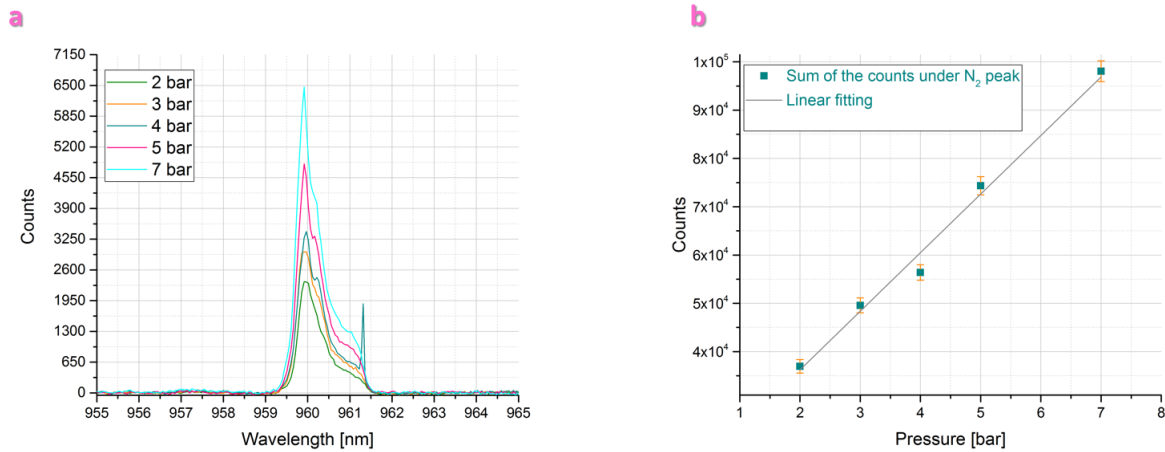
Figure 44 a) Increasing the gas pressure, the Raman peak of N_2 increased. b) ~linear growth of the sum of counts under the Nitrogen peak with the pressure (plus error bars). The uncertainties in the measurement are the ones listed in table 2.

The fibre is held in place through a series of rubber O-rings. Those rings apply pressure on the Kagome causing a loss of output power caused by micro bending of the fibre and Kagome fibres especially suffer those type of losses. We obtained P_{out}/P_{in} ratio of just 42% that must be optimized by designing new O-rings or by using a fibre with lower bend loss values.

3.7 Testing the setup with a photonic bandgap fibre

Previous measurements of spontaneous Raman scattering from a gas sample confined in a hollow core photonic crystal fibre, had all been reported in photonic bandgap fibres [1-6]. For the first time, we reported spontaneous Raman scattering from a gas sample confined in a Kagome anti-resonant fibre. To compare the two cases, we substituted the Kagome fibre we had previously used in the setup rig, with a photonic bandgap fibre working around 800nm.

The modification of the setup rig is shown in figure 45. The HC-PBGF has a 19-cells core and the core diameter is ~16 μm. To have an optimal coupling of the laser beam from the laser patchcord into the PBGF and from the PBGF to the SMA connected to the spectrometer, an arrangement of 20X and 10X lenses and two 10X lenses respectively has been used following the same principles discussed in 2.1.
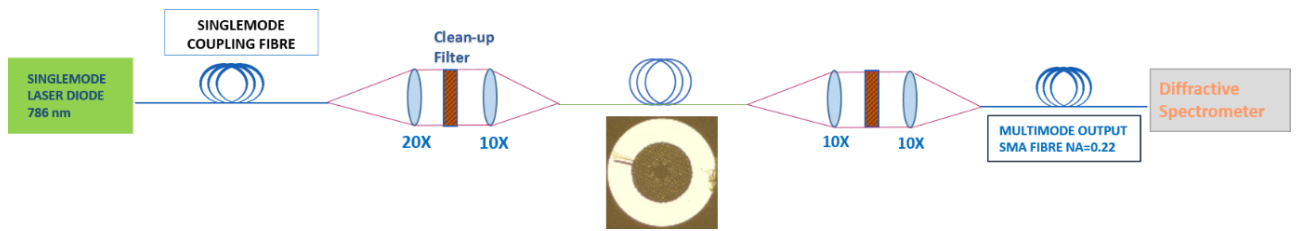
Figure 445 Setup rig modified for the PBGF. A microscope image of the fibre is also shown in the figure.

3.7.1 Initial Measurements of Spontaneous Raman Scattering from Ambient Air Contained in the PBGF

The bottom graph of figure 45 shows the result of Raman scattering from ambient air contained in 2.7m of the PBGF using 50mW of laser power and 60s of integration time. It is possible to see the O_2 peak and a surprisingly clear peak of N_2 considering the high fibre loss value expected at the Nitrogen line (as reported in 2.4.2). The top of figure 45 shows the result of the scattering with the same parameters but using the Kagome fibre. The silica Raman contribution that is observable between 860 and 880nm of the plots, is lower in the Kagome, whose guidance mechanism entails less overlap of the guided light with the core membrane. Furthermore, the core of the Kagome is bigger than the PBGF one (~50μm versus the small ~16μm core of the PBGF), allowing an easier coupling of the light in the core of the fibre.
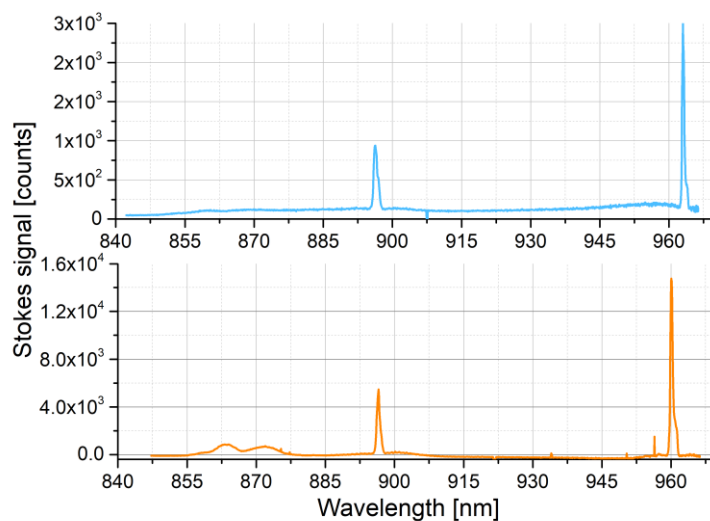
Figure 45 Raman spectrum of ambient air contained into 2.7 m of K-HCF (top) and 2.7 m of HC-PBGF (bottom) for a coupled laser power of ~ 50 mW. The peaks of oxygen Stokes signal at ~896 nm and nitrogen Stokes at ~ 962 nm are evident. Silica Raman signal can be observed between 860 and 880 nm in the HC-PBGF [12].

In figure 46, it is shown the evolution of the Stokes signals of Nitrogen and Oxygen for both fibres as a function of the laser power (top of the figure) and of the power coupled into the core (bottom). The coupled power is estimated using the fibre loss at the pump laser wavelength

(~170dB/km at 786.4nm). The coupling efficiency was of ~90% for the Kagome, around 50% for the PBGF.
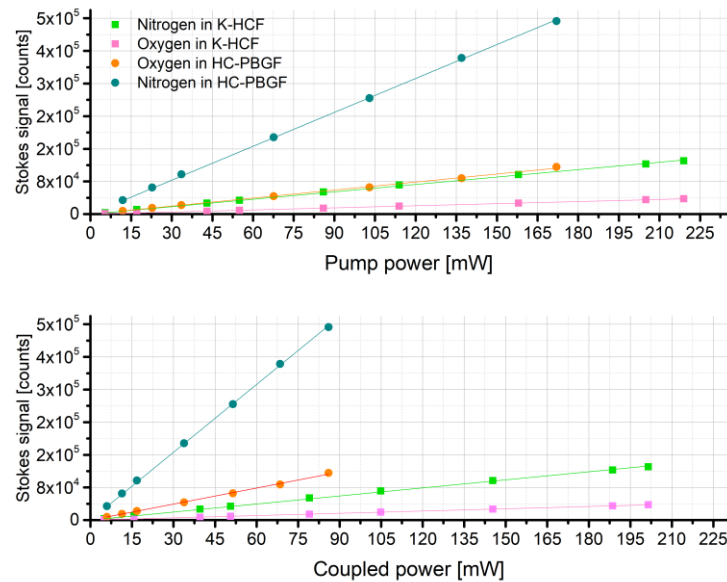
Figure 46 Evolution of Raman Stokes signals in HC-PBGF and Kagome-HCF versus laser power (top) and laser power coupled into the fibres(bottom) [12].

Both figure 45 and 46 show the Oxygen and Nitrogen Stokes signals are stronger in the PBGF case, especially if the coupled power is considered. The strength of the Nitrogen Stokes is particularly unexpected, as the loss of the fibre at the N_2 Raman line (962.91nm) and at the pump wavelength is much higher in the PBGF than in the Kagome.

All the results exposed in this section have been published in [12]. To further analyse and understand the unexpected behaviour of Nitrogen, other experiments have been run using the PBGF. The results will be discussed in the next section.

3.7.2 PBGF as gas cell: further experiments

Before running the new measurements, simulations have been performed in Matlab to predict and evaluate, the performance of setup. The simulations are based on the equations describing Raman scattering from a gas contained in a hollow core fibre and on the loss values at the pump and Raman wavelengths already reported in 2.4.2. Figure 47 shows the evolution of the Stokes powers with the fibre length. From the simulations, the maximum Stokes power expected for N_2 and O_2 is at ~14m and ~31m respectively.
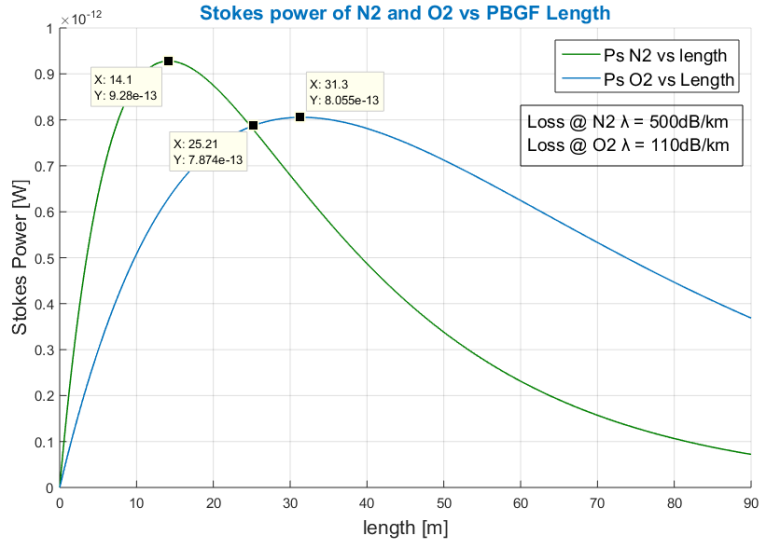
Figure 47 Simulation of Stokes power vs fibre length showing the maximum for Nitrogen and Oxygen at ~14m and ~31m respectively.

The first set of experiments have been done using 2.4m and 29m of PBGF containing ambient air. Considering the Stokes power equation for hollow core fibre (22), the expected Stokes Power ratio between O_2 and N_2 (resulting from the simulations) was ~0.955 for 29m PBGF and ~2.62 for 2.4m PBGF. The NA at the Raman wavelengths has been assumed ~0.13 from calculations presents in literature [60]. The assumption is not exactly true, as the NA of the PBGF should changes with the wavelength [60]. This effect will be discussed later on.

To compare the strength of the O_2 and N_2 Raman signal, the sums of the counts under each Raman peak have been calculated and plotted versus the coupled power as shown in figure 48. The ratio between the slopes of the linear fit applied to each set of data did not match the simulation values and was 2.9 for both lengths. Here, all the spectra have been acquired with an integration time of 30s. It was surprising to see the Nitrogen Stokes strength considering the high attenuation of the PBGF at the Nitrogen Raman wavelength.
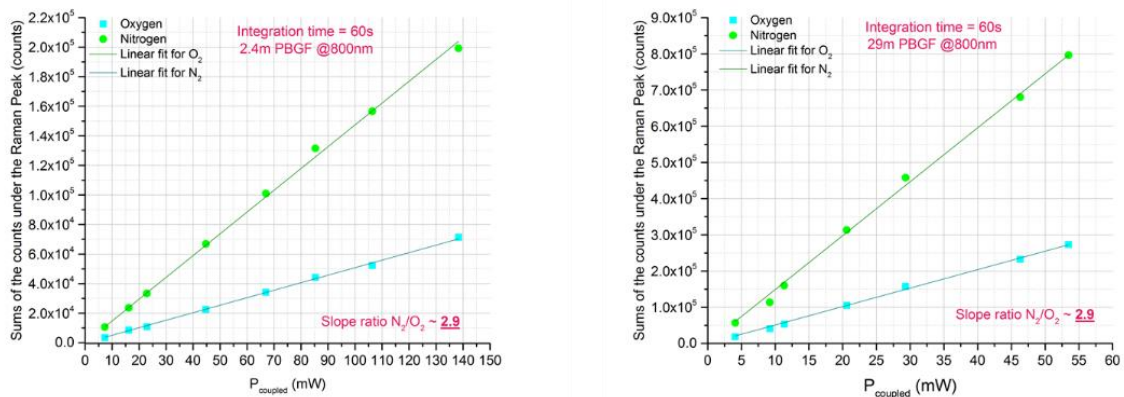
Figure 48 Evolution of the sums of the counts under each Raman peak of N_2 and O_2 increasing the power coupled into 2.4m (left) and 29m (right) PBGF. The figure shows the ratio value between the slopes of the linear fits for both the gases and the fibre lengths considered.

To have a better understanding of this event, a series of cutback-like measurement from 29m to 3.8m of PBGF has been run to obtain, experimentally, the evolution of the Stokes power with the fibre length. 5m of fibre has been cut off repeatedly to the final length of 3.8m and the Raman spectra of the ambient air increasing the laser power has been acquired for each length. The result of these cutback-like measurements is shown in figure 49, in which the sums of the counts under each Raman line vs coupled power are shown with their linear fit for each length of PBGF.
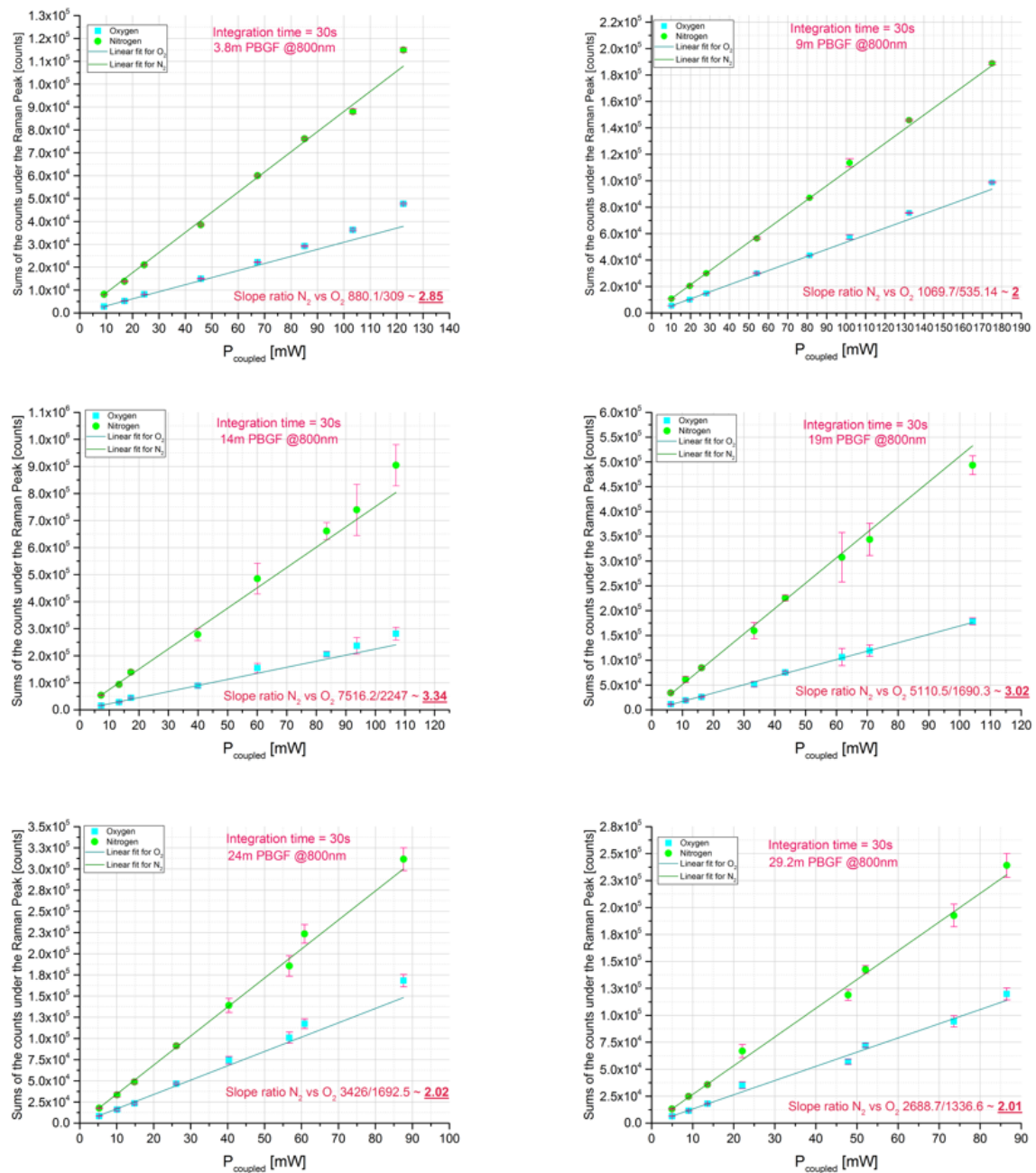
Figure 49 Sum of the counts under the Raman peaks of N₂ and O₂ vs power coupled into the PBGF with error bars and linear fits. The data have been acquired cutting back repeatedly the fibre from 29.2m (top left) to 3.8m (bottom right) of 5m each time.

Like in the previous experiments with 2.4m and 29m of PBGF, it is possible to notice the unexpected strength of the Nitrogen Raman signal even in the 29.2m length case, where the simulations predicted the Oxygen Raman line would have been stronger than the Nitrogen one and would have had a maximum (see figure 47). The coupled power has been calculated knowing the power at the output of the PBGF and the loss of the fibre for the specific length and the error bars included in the plots point out the large fluctuations experienced by the output power.

All the data collected in the latter set of measurements (cutting back the fibre from 29.2m to 3.8m) have been used to experimentally re-create the plot of figure 47. The Y-axes of figure 50 represents the slopes of the linear fits shown in figure 49. The shape of both the plots for Nitrogen and Oxygen well-resemble the one in Fig.47, but as already observed before, the Nitrogen Stokes lines seem not to experience the high attenuation predicted by the loss measurement for the fibre (figure 23, chapter 2). Moreover, the maximum of the Oxygen Raman line is not placed at ~30m as in the simulations.
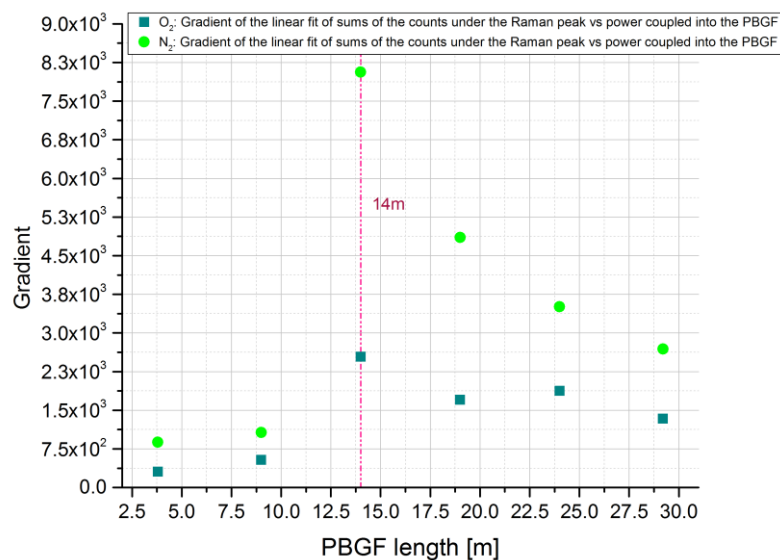
Figure 50 Evolution of the linear fit slopes of figure 46 versus the PBGF length for N2 and O₂.

The conflicting results about the strengths of the Raman lines, led to some doubts about the transmission and loss of the fibre shown in figure 23. Therefore, both have been tested again using a white light source and recording the output with the OSA and with the spectrometer as shown in figure 51. The loss of the fibre has been approximated considering the transmission of two pieces of fibres (~3.4m and ~28.5m).
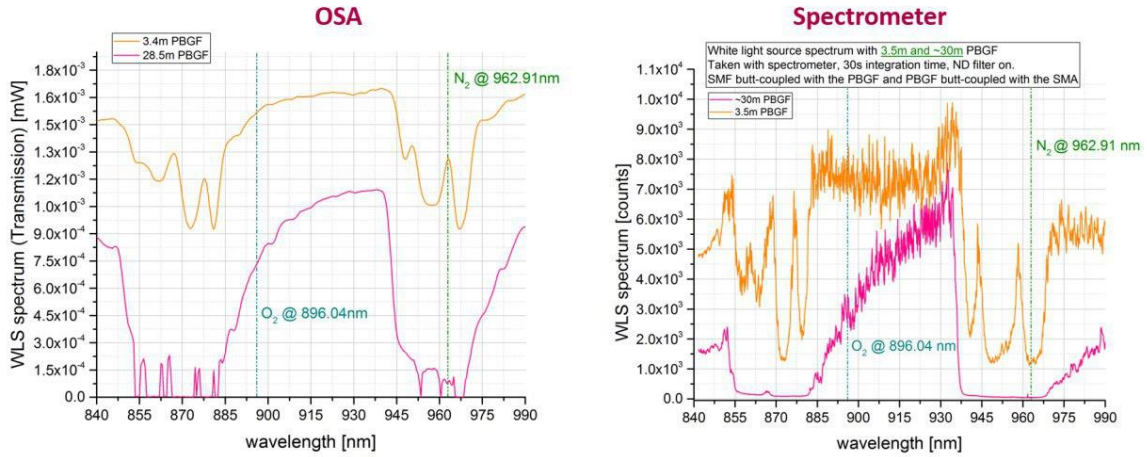
Figure 51 Transmission of the white light source through ~3.4m and ~28.5m PBGF as recorded by the OSA and the diffractive spectrometer.

The loss values for the laser pump at 786.4nm and for the Oxygen Raman line at 896.04nm seem to be higher than the one reported in the previous loss measurements (figure 23). This fact may explain why the maximum of the O_2 stokes power is shifted towards shorter lengths of fibre. More important, the results depicted in figure 51 prove once again that the Nitrogen Raman line at 962.91nm should experience high attenuation along the fibre. However, its position on the bandgap edge makes the understanding of the actual behaviour difficult due to the presence of surface modes; already discussed in 1.4. Considering the PBGF used in the experiments, figures 23 and 51 have shown Nitrogen Raman line lies in the high loss region caused by the surface modes. We speculate that the fundamental mode might not be guided anymore in this region and the Raman scattering from Nitrogen is coupled in high order core-modes. Contrary to what we normally expect, it may be possible in these limited spectral regions that the higher order modes have lower loss than the fundamental mode. It is also important to point out the aspect regarding the NA concept in the hollow core fibres. We assumed in the simulations, that the numerical aperture of nitrogen has the same value of the Oxygen one (~0.13). However, as already exposed in 2.4.2, the numerical aperture of hollow core fibres is actually a function of frequency [60]. Due to all those aspects, Raman scattering from Nitrogen in the PBGF would require further investigation in a fibre designed to operate with a transmission window better suited to the Nitrogen Stoke line.

3.7.3 Comparison between Kagome fibre and PBGF

The comparison of the Raman Stokes signals from the 7-cell Kagome fibre and from the PBGF is shown in figure 52. Due to the uncertainty about the Stokes signal at the Nitrogen wavelength for the PBGF, it has been decided to compare just the Oxygen lines. Two similar lengths have been considered for both the fibres, 2.7m and 27m of Kagome, 3.8m and 29.5m of PBGF. The results well-match what has been previously demonstrated in [12] for the short lengths, spontaneous Raman scattering signal from the PBGF is ~3 times stronger than the one from Kagome. Considering the longer lengths, the comparison shows a slightly stronger signal obtained in the Kagome, while the signals increase of 7.6 times in the Kagome and just 2.27 in

the PBGF. This difference is due to the much higher attenuation experienced by the O_2 Raman wavelength in the PBGF (~250dB/km from Fig. 48b) than in the Kagome (~100dB/km) and to the different coupling efficiency in the two fibres (~90% into the Kagome, max 45% into the PBGF).

The relatively low coupling efficiency obtained and the large oscillations observed in the output signal of the PBGF (see the error bars in Fig.52) has led to some questions about the state of the fibre itself. PBGFs are in general subjected to contamination from the ambient and the fibre used in the experiments was drawn in 2013 and let exposed to the air since then. The interaction of the contaminant with the fibre might have led to chemical reactions causing defects in the cladding and core surround and thus leading to change in the transmission and loss of the PBGF.

The Carbon Dioxide Raman lines observed in the Kagome fibre (see 3.6) cannot be seen with the current PBGF. The low concentration of CO_2 in ambient air and the high loss region in which its Raman lines lie (874.87nm and 882.75nm), make the signal too weak to be acquired by the spectrometer.
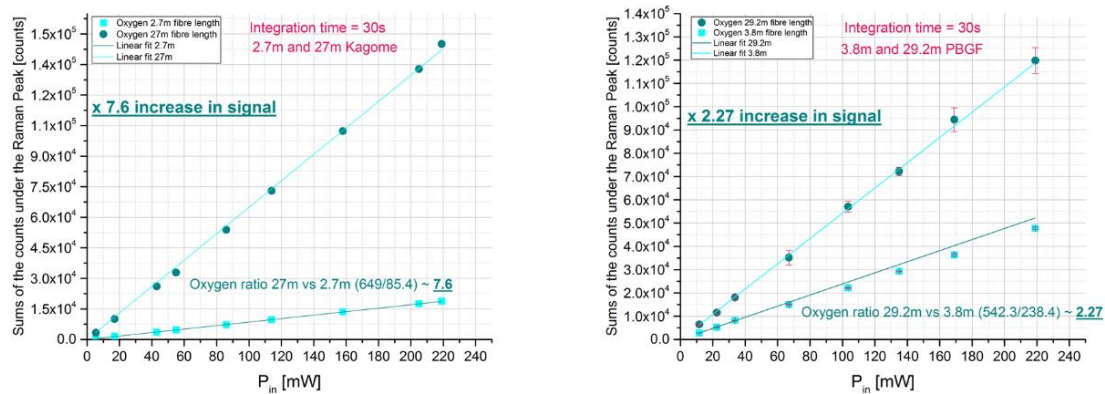

Figure 52 Counts under the O_2 Raman peak of Oxygen vs input pump power in 2.7m and 27m 7-cells Kagome (left), and in 3.8m and 29.2m PBGF (right) with the linear fits. The error bars in the PBGF plots point out the flickering of the output power from which the input power is estimated.

Conclusion

With IS-Instruments, the industrial sponsor for this project, we designed and built what can be defined as the backbone of a novel gas sensor, a device that has high potential and may cover a vast range of applications. The gas sensor was designed to be capable of high sensitivity and selectivity, with potential for fast (tens of seconds) and in-field measurements. It had also to be able to detect one or more gases from a mixture, providing information on possible contaminations or dangerous leaks. One of the applications IS-Instruments was particularly interested in, is the use of the sensor in the high pressurized (90 bar) gas pipelines. Today, the most used technique for gas detection in the gas pipelines application is Gas Chromatography, a technique that exploits chemical reactions to separate and distinguish the components of a mixture of gases. The main drawback is the necessity to extract a sample from the environment under test (the pipeline for instance) and pre-treat before it is analysed in a lab [61]. We designed a sensor that could be used directly inside the pipelines, based on a (optical) sensing technique that did not need pre-treating of the sample under test. A Raman effect-based gas sensor well met those requirements as Raman scattering from a gas mixture can detect and distinguish the single gases contained using a single excitation wavelength. Furthermore, since the Raman lines intensity are proportional to the pressure of the gas, the sensor may exploit the high pressure of the gas pipeline, making this a positive rather than a negative. We decided to use hollow core fibres as the gas cell, to exploit the long interaction length (corresponding to the fibre length) between the gas contained in the hollow core and the light travelling within. These fibres have been previously tested at high pressures and shown to withstand up to 150 bar [62]. Moreover, the fibre itself could potentially be used as in-field probe for a real-time measurement without a need for sample extraction.

All previously published works describing gas sensing based on spontaneous Raman scattering in hollow core fibres, used hollow core photonic bandgap fibres (HC-PBGFs). We have demonstrated for the first time, spontaneous Raman scattering from gases contained in a Kagome fibre, a different type of hollow core fibre, whose guidance mechanism is quite different from a HC-PBGF [12] leading to optical properties, such as lower loss at wavelengths below 1 um and wider operating bandwidth than HC-PBGF, which may prove advantageous for our application.

In the experiments, the Kagome fibre was tested filled with ambient air at 1 bar and later with a mixture of N_2 and CO_2 at 1% to perform first high-pressure experiments. The results were in good agreement with the simulations, moreover, during the ambient air measurements at 1 bar, the sensor could detect Raman scattering from CO_2 in 27m of fibre, a gas present in ambient air with a concentration of just 0.04%. The detection of Carbon Dioxide proved the current sensitivity of the system corresponding to some hundreds of ppm (~380ppm).

Subsequent experiments with a HC-PBGF, with a guidance window centred around 800 nm, were run to compare the performance of the two types of fibres. The experiments showed a ~3.7 times stronger Raman signal in the HC-PBGF than in the Kagome, using relatively short lengths of fibres (~3m); even considering the lower coupling efficiency obtained in the PBGF

than in the Kagome (<50% against ~90%), the Photonic Bandgap fibre still outperforms the Kagome one. The lower transmission loss of the Kagome fibre at the pump and stokes lines, suggests that the significantly higher numerical aperture of the PBGF, play a significant role in these results.

All the previous works on Raman gas sensing based on hollow core fibres, have been done using short fibre lengths (50cm to ~3m). This could be an advantage when it comes to build an inexpensive and portable device. However, for high-sensitivity applications, like in industrial environments or for the monitoring of the gas pipelines, the cost and the size may not be the driving factors of the design. The final goals are reliability and competitiveness, from a performance standpoint, with other gas sensing techniques currently leading the market of interest; in such, sensitivity is a key factor. The measurements with longer fibres (~28m) showed a stronger signal to length increase of the Stokes intensities for the Kagome compared to the HC-PBGF case (7.6-fold increase for the Kagome versus ~2-fold increase for the HC-PBGF) due to the lower transmission loss of the Kagome. Allowing for a longer fibre length, the Kagome could potentially be exploited to reach higher sensitivity. However, lower transmission loss at the wavelengths of interest, could be potentially achieved in a new, custom-drawn PBGF, even though drawing PBGF fibres working at ~ 800nm is more challenging than drawing fibres working at higher wavelengths [63]; moreover, they present higher attenuation due to the λ^{-3} surface scattering attenuation-dependence.

During the analysis of the data collected from the experiments, it has been noticed that the background noise and the silica Raman noise represent an issue for the detection of weak signals. It is theoretically possible to reduce or subtract the noise coming from the external ambient (dark spectrum) once it has been characterized. Silica Raman noise, on the other hand, has a wideband effect that in the ambient air experiments, for instance, extends in the wavelength range of the first CO_2 Raman line. Having silica Raman noise means the light is not guided entirely in the core of the fibres, but it also travels in the silica cladding structure, and this effect is stronger in the PBGF than in the Kagome. To reduce this noise, the launch conditions need to be optimized. Being able to see where the light is guided and what kind of modes are excited, would be crucial to achieve the proper adjustment of the launch.

Additional investigations must be done to determine in what conditions, in terms of fibre attenuation and fibre length, a Kagome anti-resonant fibre could compete and possibly overcome a PBGF, by taking advantage of the lower silica noise and the wide bandwidth offered by this fibre design.

To conclude, several paths need to be explored to improve the design of the Raman gas sensor we have started developing. However, we did prove the concept behind our project and we did prove its flexibility and its potential in terms of sensitivity, selectivity and dynamic range.

Appendix A

Gas sensing methods based on change of electrical properties

There are two main families of gas sensing techniques: one based on variation of electrical properties and the other one based on other kind of variation (optics methods, gas chromatograph, calorimetric methods and so on). [64]

The most used materials for gas sensing based on change of electrical properties are the metal oxide semiconductors (MOS). SnO_2-based ones are the most sensitive and thus, the most popular for gas sensing applications among those materials. MOS-based materials detect gas through a redox reaction between the oxide surface and the gas sample. The reaction causes an electronic variation on the oxide surface that leads to a change in the electrical resistance of the sensing device that can be detected. SnO_2-based sensors have a specific working temperature range (from 25° to 500°), and the best temperature for a good detection changes with the gas specimen. For this reason, they might be an issue with the selectivity of the gas sensor, when, for instance, the temperature is good to detect a certain gas, but far away to the optimal value for another one. Furthermore, a certain kind of gas might require high temperature to be detected and this made those type of sensors more complicated to be used compared with other devices working at room temperature. Another important issue of the metal oxide semiconductors-based sensors is the reversibility. It takes a long recovery time for them to return to the initial conditions after each exposure to the gas. For those reasons, they are not good in some application where the concentrations of gases change rapidly.

Some kinds of volatile organic compounds (VOCs) used in household products or in industrial process, which can be easily breathed by humans, can be dangerous over a certain threshold that cannot be detected by MOS. In order to detect those kind of compound (but also aromatic and halogenated compounds, alcohol and solvent vapours) polymer-based sensors are used. When the polymer layers are exposed to the gas analyte, some physical properties of the layer change as consequence of gas absorption. The advantages of these sensors are the high sensitivity and short response time. They operate at room temperature so they consume less energy than the MOS-based sensors, thus they can be used for battery-driven and portable units. Unfortunately, they present long-time instability, irreversibility and poor selectivity.

Another class of gas sensors popular for their sensitivity are the carbon nanotubes (CNTs). They are extremely sensitive to small amount of gases, like CO_2 and Ammonia, at room temperature. CNTs are divided in single-walled CNTs and multiwall CNTs. The first type is used in RFID tag antennas for toxic gas sensing. If the concentration of Ammonia (for instance) reach the 4%, the RFID reader can easily detect the backscattered power from the tag antenna. Multiwall CNTs are mostly used for remote detection of CO_2 and Ammonia and they are based on the change of the Nano-tube conductivity and permittivity. Like the previous types of gas sensors, in CNTs have different response time and properties (like the reversibility) depending on the gas under test [64].

In conclusion, those techniques based on sensing materials have several good advantages, like low cost and high sensitivity, especially to certain kind of gases like CO_2, Ammonia or VOCs. However, they are not the ideal tools for the detection of gas mixtures and, in the case of MOS and Polymer-based sensors, the reversibility property (necessity of long time of recovery or even irreversibility) becomes a significant issue.

Bibliography

[1] M. P. Buric, K. P. Chen, J. Falk, and a. S. D. Woodruff, "Enhanced spontaneous Raman scattering and gas composition analysis using a photonic crystal fiber", Applied Optics, vol. 47, pp. 4255-4261, Aug 10 2008.

[2] Michael P. Buric, Kevin P. Chen, Joel Falk, and Steven D. Woodruff, "Improved sensitivity gas detection by spontaneous Raman scattering", Applied Optics, vol. 48, 2009.

[3] R. Chen, P. J. Corellas, R. G. A. Zribia, A. Verta, R. Potyrailoa, and M. Ballerb, "Photonic bandgap fiber enabled Raman detection of nitrogen gas", presented at the Photonic Microdevices/Microstructures for Sensing, 2009.

[4] K. K. Chow, M. Short, S. Lam, A. McWilliams, and H. Zeng "A Raman cell based on hollow core photonic crystal fiber for human breath analysis", Med Phys, vol. 41, p. 092701, Sep 2014.

[5] R. K. Stefan Hanf, Di Yan, Jürgen Popp and Torsten Frosch, "Fiber-Enhanced Raman Multigas Spectroscopy: A Versatile Tool for Environmental Gas Sensing and Breath Analysis", Analytical Chemistry vol. 86, p. 5278−5285, 2014.

[6] Tobias Jochum, Leila Rahal, Renè J. Suckert, Jürgen Poppa, and T. Frosch, "All-in-one: a versatile gas sensor based on fiber enhanced Raman spectroscopy for monitoring postharvest fruit conservation and ripening", Analyst, vol. 141, pp. 2023-9, Mar 21 2016.

[7] C. B. Armin Lambrecht, Johannes Herbst, Frank Kuhnemann, Vincenz Sandfort and Sebastian Wolf, "Neue Methoden der laserbasierten Gasanalytik", Chemie Ingenieur Technik, vol. 88, pp. 1-11, 2016.

[8] H.A. Hyatt, J. M. Cherlow, W. R. Fenner, and S. P. S. Porto, "Cross section for the Raman effect in molecular nitrogen gas", Journal of the Optical Society of America, vol. 63, pp. 1604-1606, 1973.

[9] M. P. Buric, "Gas Phase Raman Spectroscopy Using Hollow Waveguides," Doctor of Philosophy in Electrical Engineering, Swanson School of Engineering, University of Pittsburgh, 2010.

[10] J. C. Knight, J. Broeng, T. A. Birks, and P. St. J. Russell, "Photonic Band Gap Guidance in Optical Fibers", Science, vol. 282, pp. 1476-1478, 1998.

[11] R. F. Cregan, B. J. Mangan, J. C. Knight, T. A. Birks, P. St. J. Russell, P. J. Roberts, and D. C. Allan, "Single-Mode Photonic Band Gap Guidance of Light in Air", Science, vol. 285, pp. 1537-1539, 1999.

[12] N.V. Wheeler, M. G. Pappa, T.D. Bradley, Y. Chen, W. Brooks, J. Storey, M. Foster, D.J. Richardson, and M.N. Petrovich, "Spontaneous Raman Scattering in Hollow Core Photonic Crystal Fibres", presented at IEEE Sensors Conference, 2017.

[13] G. D. Ewen Smith, Modern Raman Spectroscopy – A Practical Approach, 2005.

[14] H. A. H. Wayne R. Fenner, John M. Kellam, S.P.S. Porto, "Raman cross section of some simple gases," Journal of the Optical Society of America, vol. 63, pp. 73-77, 1973.

[15] Sharpe S W, Johnson T J, Sams R L, Chu P M, Rhoderick G C, and Johnson P A, "Gas-phase databases for quantitative infrared spectroscopy", Appl. Spectrosc., vol. 58, pp. 1452-61, Dec 2004.

[16] L. S. Rothman, "The HITRAN 2008 molecular spectroscopic database," Journal of Quantitative Spectroscopy and Radiative Transfer, vol. 110, pp. 532-572, 2009.

[17] Jane Hodgkinson and Ralph P Tatam, "Optical gas sensing: a review", Measurement Science and Technology, vol. 24, p. 012004, 2012.

[18] Peter Werle, Franz Slemr, Karl Maurer, Robert Kormann, Robert Mucke, and Bernd J.anker, "Near- and mid-infrared laser-optical sensors for gas analysis", Optics and Lasers in Engineering, vol. 37, pp. 101–114, 2002.

[19] J. Reid and D. Labrie, "Second-Harmonic Detection with Tunable Diode Lasers - Comparison of Experiment and Theory", Applied Physics vol. B 26, pp. 203-210, 1981.

[20] Chayan Mitra and Rachit Sharma, Diode Laser-Based Sensors for Extreme Harsh Environment Data Acquisition", InTech, 2016.

[21] Shuk Pavel and Jantz Robert, "Oxygen gas sensing technologies: A comprehensive review", 9th International Conference on Sensing Technology (ICST), 2015, pp. 12-17.

[22] G. Herzberg, Infrared and Raman Spectra of Polyatomic Molecules, 1945.

[23] John R. Ferraro, Kazuo Nakamoto, and Chris W. Brown, Introductory Raman Spectroscopy (Second edition), 2003.

[24] D. Long, The Raman Effect: A Unified Treatment of the Theory of Raman Scattering by Molecules, 2002.

[25] J. M. Hollas, Basic Atomic and Molecular Spectroscopy, 2002.

[26] D. Fouche and R. Chang, "Relative Raman cross section for O_3, CH_4, C_3H_8, NO, N_2O, and H_2", Applied Physics Letters, vol. 20, pp. 256-257, 1972.

[27] D. Fouche and R. Chang, "Relative Raman cross section for N_2, O_2, CO, CO_2, SO_2, and H_2S", Applied Physics Letters, vol. 18, pp. 579-580, 1971.

[28] Wayne R. Fenner, Howard A. Hyatt, John M. Kellam, and S.P.S. Porto, "Raman cross section of some simple gases", Journal of the Optical Society of America, vol. 63, 1973.

[29] C. A. Tulk, J. A. Ripmeester, and D. D. Klug, "The application of Raman spectroscopy to the study of gas hydrates", Gas Hydrates: Challenges for the Future, vol. 912, pp. 859-872, 2000.

[30] Ji-Xin Cheng and X. Sunney Xie, Coherent Raman Scattering Microscopy, 2013.

[31] M. G. Pappa, "The Development of Raman Gas Sensors based on Hollow Core Fibre Technology - Eight-Month Report," Optoelectronic Research Centre, University of Southampton, 2016.

[32] F. Benabid and P. J. Roberts, "Linear and nonlinear optical properties of hollow core photonic crystal fiber", Journal of Modern Optics, vol. 58, pp. 87-124, 2011.

[33] F. Poletti, "Nested antiresonant nodeless hollow core fiber", Optics Express, vol. 22, pp. 23807-28, Oct 06 2014.

[34] Francesco Poletti, Marco N. Petrovich, and David J. Richardson, "Hollow-core photonic bandgap fibers: technology and applications", Nanophotonics, vol. 2, pp. 315-340, 2013.

[35] F. L. Mangan BJ, Langford A, Roberts PJ. , "Low loss (1.7 dB/km) hollow core photonic bandgap fiber", presented at the Fiber Communication Conference (OFC), 2004.

[36] C. F. Roberts PJ, Sabert H, Mangan BJ, Williams DP, Farr L, Mason MW, Tomlinson A, Birks TA, Knight JC, St. Russell PJ, "Ultimate low loss of hollow-core photonic crystal fibres", Optics Express, vol. 13, pp. 236-44, 2005.

[37] W. D. Roberts PJ, Mangan BJ, Sabert H, Couny F, Wadsworth WJ, Birks TA, Knight JC, St. Russell PJ, "Realizing low loss air core photonic crystal fibers by exploiting an antiresonant core surround", Optics Express, vol. 13, pp. 8277-85, 2005.

[38] E. N. Fokoua and F. Poletti, "Understanding the Physical Origin of Surface Modes and Practical Rules for their Suppression", presented at the ECOC, 2013.

[39] F. Poletti and E. N. Fokoua, "Understanding the physical origin of surface modes and practical rules for their suppression", presented at the Optical Communication 39th European Conference and Exhibition on Optical Communication (ECOC 2013), 2013.

[40] Y.-m. Jung, V. Sleiffer, N. Baddela, M. Petrovich, J. R. Hayes, N. Wheeler, D. Gray, E. N. Fokoua, J. Wooler, and N.-L. Wong, "First demonstration of a broadband 37-cell hollow core photonic bandgap fiber and its application to high capacity mode division multiplexing", in Optical Fiber Communication Conference and Exposition and the National Fiber Optic Engineers Conference (OFC/NFOEC), 2013, 2013, pp. 1-3.

[41] J. A. West, C. M. Smith, N. F. Borrelli, D. C. Allan, and K. W. Koch, "Surface modes in air-core photonic band-gap fibers", Optics Express, vol. 12, pp. 1485-1496, 2004.

[42] Amezcua-Correa R., Broderick N.G., Petrovich M.N., Poletti F., and Richardson D.J., "Design of 7 and 19 cells core air-guiding photonic crystal fibers for low-loss, wide bandwidth and dispersion controlled operation", Optics Express, vol. 15, pp. 17577–86, Dec 24 2007.

[43] B. N. Amezcua-Correa R., Petrovich M.N., Poletti F., Richardson D.J., "Optimizing the usable bandwidth and loss through core design in realistic hollow-core photonic bandgap fibers", Optics Express, vol. 14, pp. 7974–85, 2006.

[44] Sébastien Février, Benoît Beaudou, and Pierre Viale, "Understanding origin of loss in large pitch hollow-core photonic crystal fibers and their design simplification", Optics Express, vol. 18, 2010.

[45] F. Couny, F. Benabid, P. J. Roberts, P. S. Light, and M. G. Raymer, "Generation and Photonic Guidance of Multi-Octave Optical-Frequency Combs", Science, vol. 318, pp. 1118-1121, Nov 16 2007.

[46] Y. Y. Wang, N. V. Wheeler, F. Couny, P. J. Roberts, and F. Benabid, "Low loss broadband transmission in hypocycloid-core Kagome hollow-core photonic crystal fiber", Optics Letters, vol. 36, 2010.

[47] Fei Yu, William J. Wadsworth, and Jonathan C. Knight, "Low loss silica hollow core fibers for 3–4 μm spectral region", Optics Express, vol. 20, 2012.

[48] B. Debord, M. Alharbi, A. Benoît, D. Ghosh, M. Dontabactouny, L. Vincetti, J.M. Blondy, F. Gérôme, and F. Benabid, "Ultra low-loss hypocycloid-core Kagome hollow-core photonic crystal fiber for green spectral-range applications", Optics Letters, vol. 39, 2014.

[49] B. Debord, A. Amsanpally, M. Chafer, A. Baz, M. Maurel, J. Blondy, E. Hugonnot, F. Scol, L. Vincetti, and F. Gérôme, "Ultralow transmission loss in inhibited-coupling guiding hollow fibers", Optica, vol. 4, pp. 209-217, 2017.

[50] S. Afshar, Y. Ruan, S. C. Warren-Smith, and T. M. Monro, "Enhanced fluorescence sensing using microstructured optical fibers: a comparison of forward and backward collection modes", Opt. Lett., vol. 33, pp. 1473–1475, 2008.

[51] M. Phillips, R. N. Cataneo, A. R. Cummin, A. J. Gagliardi, K. Gleeson, J. Greenberg, R. A. Maxfield, and W. N. Rom, "Detection of lung cancer with volatile markers in the breath", Chest, vol. 123, pp. 2115–2123, Jun 2003.

[52] C. J. Wang, A. Mbi, and M. Shepherd, "A study on breath acetone in diabetic patients using a cavity ringdown breath analyzer: Exploring correlations of breath acetone with blood glucose and glycohemoglobin A1C", IEEE Sensors Journal, vol. 10, pp. 54-63, Jan 2010.

[53] R. Altkorn, M. D. Malinsky, R. P. Van Duyne, and I. Koev, "Intensity considerations in liquid core optical fiber Raman spectroscopy", Applied Sepctroscopy, vol. 55, pp. 373-381, Apr 2001.

[54] Isabelle Dicaire, Jean-Charles Beugnot, and Luc Thévenaz, "Analytical modeling of the gas-filling dynamics in photonic crystal fibers", Applied Optics, vol. 49, 2010.

[55] Y. Chen, N. V. Wheeler, N. K. Baddela, J. R. Hayes, S. R. Sandoghchi, E. Numkam Fokoua, M. Li, F. Poletti, M. N. Petrovich, and D. J. Richardson, "Understanding Wavelength Scaling in 19-Cell Core Hollow-Core Photonic Bandgap Fibers", presented at the OFC, 2014.

[56] M. R. Thomas Rasmussen, Poul Hansen, Ole Jespersen, Nicolai Rasmussen and Bjarke Rose, "How to Design a Miniature Raman Spectrometer", Spectroscopy, vol. 30, 2015.

[57] Peter B. Catrysse and Brian A. Wandell, "Optical efficiency of image sensor pixels", J. Opt. Soc. Am. A, vol. 19, pp. 1610-1620, Aug 2002.

[58] Thomas J. Fellers and Michael W. Davidson. CCD Noise Sources and Signal-to-Noise Ratio. Available: http://hamamatsu.magnet.fsu.edu/articles/ccdsnr.html

[59] T. D. Bradley, N. V. Wheeler, G. T. Jasion, D. Gray, J. Hayes, M. A. Gouveia, S. R. Sandoghchi, Y. Chen, F. Poletti, D. Richardson, and M. Petrovich, "Modal content in hypocycloid Kagome hollow core photonic crystal fibers", Optics Express, vol. 24, pp. 15798-812, Jul 11 2016.

[60] M. J. Digonnet, H. K. Kim, G. S. Kino, and S. Fan, "Understanding air-core photonic-bandgap fibers: Analogy to conventional fibers", Journal of Lightwave Technology, vol. 23, p. 4169, 2005.

[61] R. L. Grob and E. F. Barry, Modern practice of gas chromatography: John Wiley & Sons, 2004.

[62] M. Azhar, G.K.L. Wong, W. Chang, N.Y. Joly and P. St.J. Russell, " High Pressure Gases in Hollow Core Photonic Crystal Fiber: A New Nonlinear Medium", arXiv, 2012.

[63] P. J. Mosley, W. C. Huang, M. G. Welch, B. J. Mangan, W. J. Wadsworth, and J. C. Knight "Ultrashort pulse compression and delivery in a hollow-core photonic crystal fiber at 540 nm wavelength", Optics Letters, Vol. 35, pp. 3589-3591, 2010.

[64] X. Liu, S. T. Cheng, H. Liu, S. Hu, D. Q. Zhang, and H. S. Ning, "A Survey on Gas Sensing Technology", Sensors, vol. 12, pp. 9635-9665, Jul 2012.